



Genome mining and biosynthesis of a polyketide from a biofertilizer fungus that can facilitate reductive iron assimilation in plant

Mengbin Chen^a, Qikun Liu^{b,c}, Shu-Shan Gao^a, Abbigayle E. Young^a, Steven E. Jacobsen^{b,c}, and Yi Tang^{a,d,1}

^aDepartment of Chemical and Biomolecular Engineering, University of California, Los Angeles, CA 90095; ^bDepartment of Molecular Cell and Developmental Biology, University of California, Los Angeles, CA 90095; ^cHoward Hughes Medical Institute, University of California, Los Angeles, CA 90095; and ^dDepartment of Chemistry and Biochemistry, University of California, Los Angeles, CA 90095

Edited by Chaitan Khosla, Stanford University, Stanford, CA, and accepted by Editorial Board Member Stephen J. Benkovic February 11, 2019 (received for review November 22, 2018)

Fungi have the potential to produce a large repertoire of bioactive molecules, many of which can affect the growth and development of plants. Genomic survey of sequenced biofertilizer fungi showed many secondary metabolite gene clusters are anchored by iterative polyketide synthases (IPKSs), which are multidomain enzymes noted for generating diverse small molecules. Focusing on the biofertilizer *Trichoderma harzianum* t-22, we identified and characterized a cryptic IPKS-containing cluster that synthesizes tricholignan A, a redox-active *ortho*-hydroquinone. Tricholignan A is shown to reduce Fe(III) and may play a role in promoting plant growth under iron-deficient conditions. The construction of tricholignan by a pair of collaborating IPKSs was investigated using heterologous reconstitution and biochemical studies. A regioselective methylation step is shown to be a key step in formation of the *ortho*-hydroquinone. The responsible methyltransferase (MT) is fused with an N-terminal pseudo-acyl carrier protein (ψ ACP), in which the *apo* state of the ACP is essential for methylation of the growing polyketide chain. The ψ ACP is proposed to bind to the IPKS and enable the *trans* MT to access the growing polyketide. Our studies show that a genome-driven approach to discovering bioactive natural products from biofertilizer fungi can lead to unique compounds and biosynthetic knowledge.

iterative polyketide synthase | biosynthesis | natural products | biofertilizer

Human beings have exploited beneficial plant–fungi relationships in agroecosystems since antiquity (1). Field studies, together with model plant studies, have shown that the presence of beneficial fungi can promote plant growth in challenging environments (2, 3). Fungi secrete lytic enzymes, hydrophobins, and metabolites that help plants scavenge nutrients and fight off pathogens (1). Fungal natural products are particularly important in plant–fungi interactions because of their rich biological properties (4, 5). Currently, the most practiced method to exploit beneficial natural products is to apply the producing microorganisms directly on plants or as soil amendments. A major limitation of this approach is that biosynthesis of natural products by fungi can be significantly affected by environmental variations, ranging from soil salinity to plant types. As a result, not all beneficial natural products can be produced under field conditions, while unintended production of mycotoxins may cause harm to the plants (6). A more direct approach is to identify potential metabolites that can be synthesized by fungi under axenic laboratory conditions and elucidate their mode of action, followed by application of the natural product or derivatives to the plant. Through genome sequencing and bioinformatic analysis, it is accepted that most fungi only produce a small fraction (<10%) of natural products under laboratory conditions compared with the number of biosynthetic gene clusters encoded (7). Recent advances in fungal genome mining tools have led to the specific and global activation of biosynthetic gene clusters as a step toward realizing the biosynthetic potential (8, 9). These approaches therefore hold significant promise in identifying new

fungal natural products that are beneficial to plant growth, and may lead to applications in agriculture.

Trichoderma harzianum t-22 is a biofertilizer fungus that is widely applied to plants from gardening to agriculture (1). *T. harzianum* t-22 can be found as a dissociative rhizosphere resident or plant endophyte that penetrates the outer layers of the epidermis without causing any invasive harm (10). *T. harzianum* t-22 synthesizes and secretes small molecules that are beneficial to plants, including polyketides that are pathogen antagonists and plant growth regulators (11). Genome sequencing of *T. harzianum* t-22 showed the strain encodes 25 clusters that are anchored by iterative polyketide synthases (IPKSs), far exceeding the number of known polyketides produced by this fungus. Therefore, we reasoned a genome-based approach to mine the IPKS-containing gene clusters in *T. harzianum* t-22 may reveal new natural products that play roles in plant–fungi interactions.

IPKSs are multidomain enzymes that function iteratively to synthesize the core structures of polyketides using primarily malonyl-CoA as the building block (12). While the domain arrangement of IPKSs resembles closely that of fatty acid synthases (FASs), more complex biochemical programming rules lead to diverse structures and complicate structural prediction (13). For example, the tailoring domains, including ketoreductase, dehydratase, enoylreductase, and methyltransferase (MT), function with finely tuned permutations in each iteration to diversify the

Significance

Extensively used as a biofertilizer in agriculture, *Trichoderma harzianum* t-22 has been shown to promote plant fitness via secreting small molecules that have diverse functions. Tricholignan A, discovered via genome mining in this work, is a redox-active *ortho*-hydroquinone natural product that can facilitate reductive Fe assimilation in plant. The biosynthesis of the *ortho*-hydroquinone structure by a pair of polyketide synthases (PKSs) requires a critical α -methylation step that serves as the programming checkpoint. The responsible standalone methyltransferase requires chaperoning by a fused and inactive acyl carrier protein for activity. The use of an inactive carrier protein to regulate PKS function adds another layer of complexity to this already highly enigmatic family of enzymes.

Author contributions: M.C. and Y.T. designed research; M.C., Q.L., and A.E.Y. performed research; M.C., Q.L., S.-S.G., S.E.J., and Y.T. analyzed data; and M.C. and Y.T. wrote the paper.

The authors declare no conflict of interest.

This article is a PNAS Direct Submission. C.K. is a guest editor invited by the Editorial Board.

Published under the PNAS license.

¹To whom correspondence should be addressed. Email: yitang@g.ucla.edu.

This article contains supporting information online at www.pnas.org/lookup/suppl/doi:10.1073/pnas.1819998116/-DCSupplemental.

Published online March 6, 2019.

carbon backbone (12, 13). The polyketide structure that results is typically precisely crafted to enable a multitude of post-polyketide synthase (PKS) reactions to take place and furnish the final bioactive products. Additional structural complexity can be generated through collaborative efforts between multiple IPKs, as illustrated in the biosynthesis of sorbicillin and chaetoviridin A (14, 15). In these pathways, a highly reducing IPKS (HRPKS) and a nonreducing IPKS (NRPKS) collaborate in tandem to synthesize a compound with both reduced and aromatic features. Starting from a cryptic tandem IPKS in *T. harzianum* t-22, we report here the discovery of a redox-active *ortho*-hydroquinone molecule tricholignan A **1**. Tricholignan A is able to reduce Fe(III) to Fe(II), and can alleviate iron deficiency phenotypes in the model plant *Arabidopsis thaliana*. We showed the polyketide core structure of tricholignan A is constructed via unique programming rules involving a *trans*-acting MT. Our studies therefore support the potential of genome mining in biofertilizer fungi to afford new agriculturally relevant natural products.

Results

Activating Silent *tlh* Cluster in *T. harzianum* t-22 Leads to Tricholignan A

A. We performed anti-SMASH and bioinformatic analysis of the sequenced *T. harzianum* genome to identify all IPKS-containing biosynthetic gene clusters (16). Of the 25 gene clusters identified, the *tlh* gene cluster encoding an HRPKS (TlnA) and an NRPKS (TlnB) attracted our attention (Fig. 1A) because: (i) there are genes encoding thioesterase (TE), flavin-dependent monooxygenase (FMO), and *O*-MT, which could further expand chemical diversity, and (ii) the gene *tlhC* encodes an unusual didomain protein with an N-terminal acyl carrier protein (ACP) and a C-terminal MT. Analysis of its amino acid sequence revealed that while the conserved *S*-adenosylmethionine (SAM) binding and catalytic motifs of the MT domain are present, the phosphopantetheine (pPant) modification site in the ACP domain is DTI, which deviates from the hallmark DSL sequence (17–19) (Fig. 1B). Substitution of the serine with threonine raises the possibility that this ACP domain may not be posttranslationally

modified with pPant and may be inactive. Hence, the fusion protein encoded was designated as pseudo-ACP-MT (ψ ACP-MT). RT-PCR analysis showed that the cluster was transcriptionally silent under laboratory conditions (SI Appendix, Fig. S2.1), consistent with the strain producing primarily pachybasin, which is unrelated to the *tlh* cluster (Fig. 1C, i). To activate this gene cluster, we use a transcription activation approach (8, 9). The gene *thnI*, which encodes a putative GAL4-like Zn₂Cys₆ transcription factor, was cloned under the control of the constitutive *gpdA* promoter (8). Upon integration of this cassette into *T. harzianum* to yield the strain TLB2, transcription of genes in the *tlh* cluster was activated (SI Appendix, Fig. S2.1).

Several distinctive metabolites emerged from the extract of TLB2 grown in potato dextrose broth for 4 d at 28 °C, with 1 and 2 being the major compounds (~2 mg/L) (Fig. 1C). Compounds with similar UV absorbance profiles [λ_{max} (wavelength of maximum absorption) = 222 nm, $\lambda_{\text{max}} = 279$ nm] were isolated, and the structures were determined by NMR analysis (SI Appendix, Tables S4–S8). Tricholignan A **1** is a trisubstituted *o*-hydroquinone (4-methoxy-5-methyl-6-sorbyl *o*-hydroquinone), while tricholignan B **2** is the oxidized *o*-quinone. Compounds **1** and **2** therefore form a redox pair, with **1** undergoing air oxidation to **2**. Both **1** and **2** are compounds not previously reported in the literature.

The minor metabolites identified from TLB2 that are related to **2** are putative precursors (**3** and **9**) and dimers of **1** and **2** (**4**, **4'**, and **5**). Compound **3** is a tetrasubstituted benzoic acid and is proposed to be the product of the HRPKS/NRPKS collaboration (Fig. 1). Compound **3** can undergo oxidative decarboxylation and oxidation to quinone **9** (isolated as a mixture of *o*- and *p*-quinone) (20) (Fig. 1). Compounds **4**, **4'**, and **5** are all heterodimers of **1** and **2**, and are fused by a 1,4-benzodioxin moiety derived from the cycloaddition between the sorbyl chain in **1** and the *o*-quinone in **2** (SI Appendix, Fig. S2.2). Such connectivity was observed among plant metabolites, and has been proposed to occur nonenzymatically (21).

Reduction of Fe(III) by Tricholignan A Improves Iron Acquisition by *A. thaliana*.

Ortho-hydroquinones are known to be redox-active (22). Separate analysis of metabolites in media and cells of *T. harzianum* t-22 showed that **1** and **2** are exported and accumulated extracellularly, suggesting a possible redox role in the environment. Recent studies by Sattely and coworkers (23) showed that hydroxyquinones, such as fraxetin and sideretin secreted by roots of *A. thaliana*, can help the plant assimilate Fe(II) by solubilization and reduction of Fe(III) in soil. The redox potential of the tricholignan pair was measured by cyclic voltammetry. With a standard redox potential (E^0) of 568 mV at pH 6.4 and an E^0 of 545 mV at pH 7.0 (Fig. 2A and SI Appendix, Fig. S2.3), **1** could serve as a facile electron donor to reduce Fe(III) to Fe(II) (Fig. 2A). Indeed, an iron reduction assay coupled with ferrozine showed that **1** was able to reduce Fe(III) (SI Appendix, Fig. S2.4). Iron reduction by tricholignan A is slower compared with plant-derived coumarin fraxetin (23), and both reductants are susceptible to air oxidation during iron reduction in vitro.

Having established that **1** can reduce Fe(III) to Fe(II) in vitro, we hypothesized that the observed redox activity might be biologically relevant in facilitating iron acquisition by plants. To test this potential activity of **1**, we selected the *f6'h1-1* mutant (SALK_132418C) of *A. thaliana*, which cannot synthesize scopoletin (the precursor of fraxetin and sideretin), and is therefore defective in reductive iron acquisition (23). *A. thaliana* strictly uses a reduction-based strategy to acquire Fe(II), which separates itself from the other plants that utilize phytosiderophores to chelate Fe(III) (24). Under Fe-deficient conditions, the *f6'h1* mutant exhibits mild chlorosis at pH 5.6 on agar. In the presence of 150 μ M tricholignan A, chlorosis was rescued (Fig. 2B). Given that chlorophyll content is strongly correlated to the intracellular Fe(II) concentration in plants (25), we determined chlorophyll concentrations of *f6'h1* mutant seedlings under the testing growth conditions. The mean chlorophyll content of *A. thaliana* seedlings when grown in

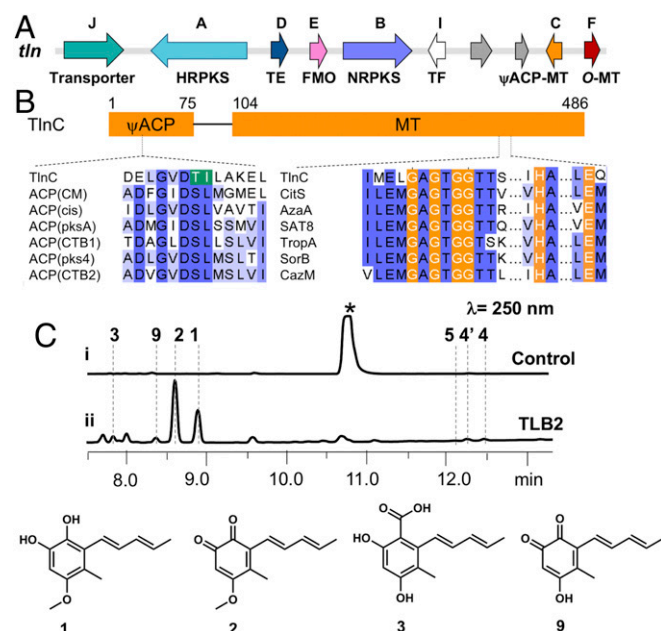


Fig. 1. Genome mining of the redox-active tricholignan from *T. harzianum* t-22. (A) Organization of the *tlh* gene cluster. TF, transcription factor. (B) Domain organization and active site motifs of TlnC. (C) Extracted LC traces of metabolite extracts from a control strain (i) and TLB2, the *tlh1* overexpression strain (ii). The asterisk represents pachybasin.

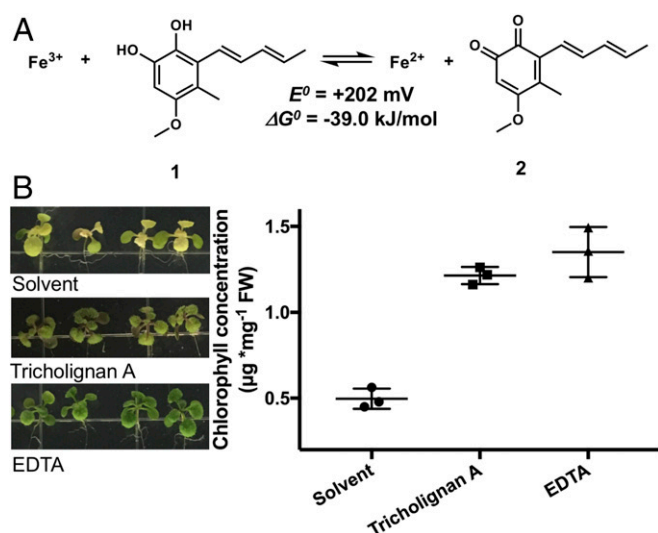


Fig. 2. Tricholignan A can facilitate reductive iron assimilation in *A. thaliana* of model plants. (A) Standard free energy changes (ΔG^0) and E^0 for ferric reduction by tricholignan A **1**. The previously reported value of +0.77 V (vs. standard hydrogen electrode) was used for ferric-to-ferrous reduction. (B) Phenotypic characterization and complementation assays for *A. thaliana* *f6'h1* mutant under Fe-deficient conditions.

the presence of tricholignan A was $1.2 \mu\text{g} \cdot \text{mg}^{-1}$ of fresh weight (FW; the unit is defined as chlorophyll concentration in micrograms per milligram of FW leaf disks), which is comparable to that of the positive control of adding EDTA. As expected, the chlorophyll content of the seedlings grown on solvent-only control was significantly lower, at around $0.5 \mu\text{g} \cdot \text{mg}^{-1}$ of FW. A previous study showed that *T. harzianum* t-22 grown in liquid culture can generate diffusible metabolites that reduce Fe(III) to Fe(II) to promote plant growth, but the molecular basis was unknown (26). Our studies suggest genome-mined **1** may be one such metabolite that can reduce Fe(III), while the biosynthesis of **1** may be activated under specific conditions.

Given the potential role of **1** in iron assimilation, we postulated that the *tnl* cluster should be found in other beneficial fungal species besides *T. harzianum* t-22. An anti-SMASH search of publicly available sequenced genomes revealed that this cluster is conserved across *Trichoderma* spp., including *Trichoderma virens*, *Trichoderma atroviride*, *Trichoderma guizhouense*, and several other *T. harzianum* variants (2, 27, 28) (SI Appendix, Fig. S2.5). These clusters encode proteins that are almost identical to the ones in the *tnl* cluster, with amino acid identities of over 80%. These fungi have been reported to promote plant growth, and the fact that the *tnl* cluster is conserved in them but absent in other fungal genera further supports its potential role in improving plant fitness.

Reconstitution of Tricholignan A Biosynthesis. The *o*-hydroxyquinone moiety of **1** is essential for the observed redox activity. Searching through known fungal natural products showed that this is rare among fungal metabolites (29). To understand the biosynthetic logic in producing *o*-hydroxyquinone via a polyketide pathway, we reconstituted the individual steps in the biosynthesis of **1** and **2**. We expressed combinations of *tnl* genes in *Saccharomyces cerevisiae* BJ5464-NpgA (30) (Fig. 3B). Whereas expression of the IPKs (TlnA and TlnB) alone or together did not yield any detectable products, coexpression of TlnD (TE) led to formation of the truncated pentaketide pyrone **7** as a major product and hexaketide β -resorcylic acid **8** as a minor product. TlnD is therefore proposed to be the TE that releases the products from TlnB via hydrolysis (Fig. 3A). Coexpression of TlnC (ψ ACP-MT) with TlnA, TlnB, and TlnD in yeast resulted in biosynthesis of **3** (Fig.

3B), thereby confirming the MT domain is active and is responsible for C5-methylation in **1**–**3**.

Starting from the yeast strain that produced **3**, further coexpression of TlnE (FMO) and TlnF (*O*-MT) produced **2** ($\sim 0.2 \text{ mg/L}$). The catalytic roles of TlnE and TlnF were verified using purified enzyme assays (SI Appendix, Fig. S2.6). In the presence of both enzymes, NADPH and SAM, **3** is converted to **2** (SI Appendix, Fig. S2.6, v). The sequence of reactions was established by adding enzymes individually in the assay. Incubating **3** and NADPH with TlnE yielded **9** (and **9'**) (SI Appendix, Fig. S2.6, iii). We were not able to detect the reduced intermediate **10**, likely due to rapid spontaneous air oxidation. The oxidative decarboxylation of TlnE is similar to that of salicylate hydroxylase in *Pseudomonas putida*, which catalyzes conversion of salicylic acid to catechol (31). Directly incubating **9** and SAM with TlnF led to **2** (SI Appendix, Fig. S2.6, iv). However, adding TlnF to **3** did not lead to any *O*-methylated products (SI Appendix, Fig. S2.6, ii), confirming the sequence of reactions as shown in Fig. 3A. The enzymatic conversion of **3** to **2** reveals the logic of *o*-quinone biosynthesis: Following oxidative decarboxylation by TlnE, both *o*- and *p*-quinones (**9** and **9'**) can be formed from trihydroxybenzene **10**. Methylation on the C4-phenol in **9** results in exclusive formation of the *o*-quinone **2**, mimicking the strategy used in the chemical syntheses of *o*-quinone (32).

ψ ACP Is Required for Polyketide Methylation and Biosynthesis of **3**.

To study in detail the biosynthesis of **3**, we expressed and purified TlnA, TlnB, and TlnD from yeast, as well as TlnC from *Escherichia coli* BL21(DE3) (SI Appendix, Fig. S2.15). One-pot enzymatic reaction of these four enzymes, in the presence of malonyl-CoA, NADPH, and SAM, resulted in the formation of

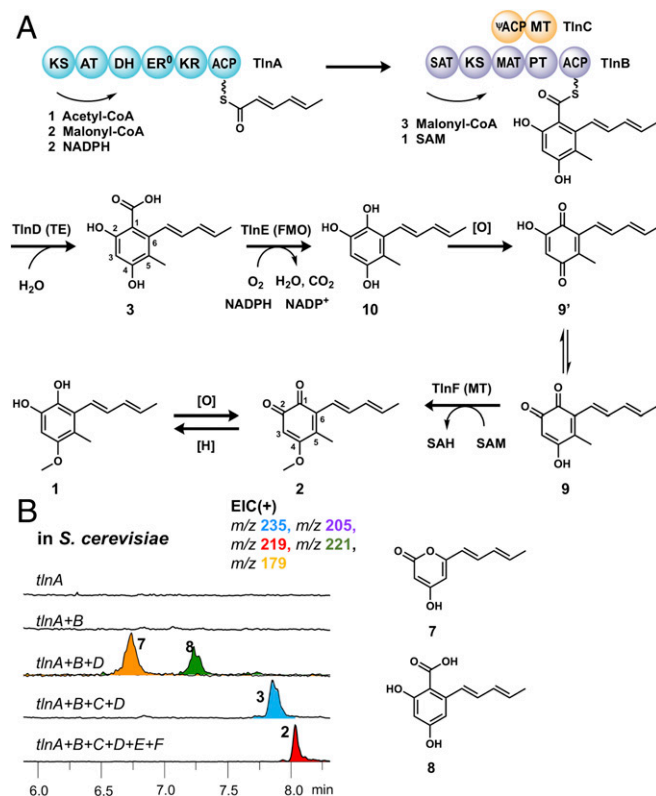


Fig. 3. Functional assignment of enzymes in the *tnl* cluster. (A) Proposed biosynthetic pathway of the *tnl* cluster. AT, acyltransferase; DH, dehydratase; ER, enoylreductase; KR, ketoreductase; PT, product template; SAH, S-adenosylhomocysteine. (B) Extracted LC/MS traces of reconstitution of TlnA through TlnF activity in *S. cerevisiae* BJ5464-NpgA. EIC, extracted ion chromatogram.

the hexaketide **3** (Fig. 4*B*, *i*), proving these four enzymes are sufficient for biosynthesis of **3**. In the absence of ψ ACP-MT TlnC, the dominant product synthesized by TlnA, TlnB, and TlnD is **7**, a spontaneously released pentaketide shunt product (Fig. 4*B*, *ii*). Only trace amounts of the 5-desmethyl **8** are formed. When purified TlnC was incubated with **8**, no methylation to **3** can be observed. These results suggest that methylation by the MT domain of TlnC must take place during TlnB-catalyzed chain elongation, and does not take place post-PKS. A proposed scheme of synthesis of **3** by the four enzymes is shown in Fig. 4*A*. The HRPKS TlnA synthesizes the triketide hexa-2,4-dienoate, which can be detected via base hydrolysis of TlnA incubated with malonyl-CoA and NADPH (*SI Appendix*, Fig. S2.7). TlnB accepts the sorbyl unit from TlnA as a starter unit via the starter unit/ACP transacylase (SAT) domain and extends to the tetraketide intermediate, which can be methylated by TlnC. Following two more rounds of chain extension by TlnB to give the hexaketide, the product template domain of TlnB catalyzes regioselective cyclization to yield the TlnB-tethered 2,4-dihydroxybenzoyl product (**33**, **34**). Finally, TlnD catalyzes hydrolytic release to yield **3** (Fig. 4*A*). In the absence of TlnC-catalyzed methylation at the tetraketide stage, TlnB programming rules are derailed and the vast majority of products are released via enolization of the ϵ -ketone and cyclization to give pyrone **7**. Only a small fraction of unmethylated polyketide can proceed fully to the hexaketide and be released as **8**. Therefore, the TlnC-catalyzed α -methylation step serves as a checkpoint in TlnB

programmed steps to ensure **3**, not **8**, is produced. α -Methylation as a checkpoint in HRPKS programming has been noted previously (35, 36), and is observed here for an NRPKS via interacting with an *in trans* MT.

To determine the role of the ψ ACP domain in the TlnC-catalyzed reaction, we excised and assayed the standalone MT domain (Δ TlnC) with TlnA, TlnB, and TlnD. While a small amount of **3** is made, the major product (>80%) is now **7**, indicating the efficiency of methylation is severely impaired without ψ ACP (Fig. 4*B*, *iii*). This is confirmed through *in trans* complementation with the standalone ψ ACP domain, which led to a small increase in **3**, but **7** is still a dominant product (Fig. 4*B*, *iv*). Hence, the presence of a fused ψ ACP significantly enhances the efficiency of the methylation step, possibly via transient protein-protein interactions with TlnB. Increasing the ratio of ψ ACP to Δ TlnC increased the relative amount of **3** to **7**, although the total polyketide yield decreased (*SI Appendix*, Fig. S2.8).

We then used MALDI-TOF analysis to determine whether the threonine residue present in the DTI motif of ψ ACP can be posttranslationally modified by the fungal phosphopantetheinyl transferase NpgA (37). When the standalone ψ ACP was treated with CoA and NpgA, the threonine remained unmodified (*SI Appendix*, Fig. S2.9). In contrast, the excised ACP domain from TlnB (ACP_{cis}) was completely phosphopantetheinylated under the same conditions. The circular dichroism (CD) spectrum of ψ ACP revealed the characteristic double-negative peaks at 208 nm and 222 nm that are also seen in the CD profile of ACP_{cis} (*SI Appendix*, Fig. S2.10), which are indicative of an intact α -helical bundle structure. Collectively, these data are consistent with a previous study in which introducing a single S36T mutation in *E. coli* FAS ACP led to the abolishment of post-translational modification (17). Therefore, the ψ ACP domain in TlnC facilitates the *in trans* methylation reaction and may be purposely kept in the *apo* form. This was further demonstrated by using the T34A TlnC mutant in the PKS assay, which produced mostly **3** (>95%) (Fig. 4*B*, *v*).

To evaluate the effects of phosphopantetheinylation of the ψ ACP domain, we first generated a T34S- ψ ACP mutant in which the serine residue is reintroduced. The *apo* T34S- ψ ACP can now be completely converted into the *holo* form by NpgA *in vitro* (*SI Appendix*, Fig. S2.9), thereby supporting that the threonine residue in ψ ACP is present to keep the ACP domain in the *apo* form. We then introduced the T34S mutation into the full-length TlnC and repeated the PKS assays. The *apo* form of T34S TlnC was slightly compromised in activity, but still produced **3** as the major product (>70%) (Fig. 4*B*, *vi*). Surprisingly, the MT activities of *holo* T34S-TlnC are nearly completely abolished, as pyrone **7** constituted over 95% of all products, with trace amounts of **8** and **3** (Fig. 4*B*, *vii*). This result confirms that the *apo* form of the ψ ACP domain is required for proper functioning of the MT domain. Since *holo* T34S-TlnC did not inhibit PKS turnover (as evident in the formation of **7**), we reason that the pPant arm in mutant ψ ACP may insert into the juxtaposed MT domain active site and effectively inhibit TlnB ACP from shuttling the tetraketide substrate (3-oxo-4,6-octadienoyl) to the MT. The use of an unphosphopantetheinylated ACP ensures that it will not compete with acyl-ACP_{cis} from TlnB for access to TlnC MT. Therefore, the ψ ACP is a decoy: It is present in the apparent inactive *apo* form and cannot serve as an acyl shuttle of polyketide chains, yet it is critical in facilitating TlnB and TlnC interactions to ensure that the regioselective methylation takes place.

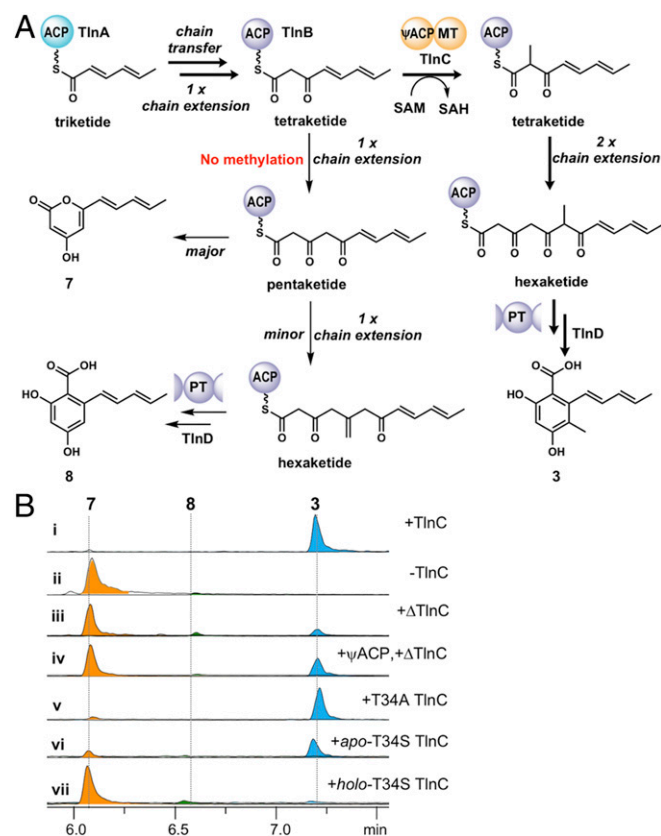


Fig. 4. ψ ACP in TlnC is essential for formation of **3**. (A) Proposed mechanism of TlnC-assisted biosynthesis of **3**. SAH, S-adenosylhomocysteine; PT, product template. (B) Extracted LC/MS traces of extracts from *in vitro* reconstitution assays with TlnA, TlnB, TlnD, and different mutants of TlnC. Δ TlnC is the truncated version in which ψ ACP is removed. The terms *apo* and *holo* indicate the absence and presence of pPant on the ACP domain, respectively. Equimolar enzyme concentrations (20–30 μ M) were used in *in vitro* assays.

ψ ACP Inhibits Decarboxylative Condensation by Ketide Synthase Domain to Facilitate Methylation. During nonreducing polyketide chain elongation by NRPKS, premature spontaneous cyclization of the reactive poly- β -ketone chain is suppressed in the active site of the NRPKS. After decarboxylative condensation between the growing polyketide chain attached to the ketide synthase

(KS) domain and an incoming malonyl-ACP, the polyketide chain may be transferred back to the KS domain and remain in the active site tunnel, or leave the active site in the form of acyl-ACP, followed by reentry and transthioesterification (38, 39). In order for MT domains to methylate α -positions, the polyketide chain must be accessible by the MT domains. In most NRPKSs that methylate polyketides, an in-line MT domain immediately fused to the ACP domain allows the MT to be in close proximity to the megasynthase core and to be accessible by acyl-ACP (36, 40). Here, TlnC is a dissociated MT enzyme that must gain access to the tetraketidyl-ACP to perform methylation. We hypothesize that ψ ACP may bind to TlnB via protein–protein interactions to recruit TlnC to the TlnB reaction core. In addition, ψ ACP may bind to the entrance of the KS active site and slow down the re-entry of the tetraketidyl-ACP_{cis} before methylation (Fig. 5D). In this case, an increased ratio of ψ ACP to TlnB should inhibit NRPKS activity, which was observed in the *in trans* complementation assay of Δ TlnC (SI Appendix, Fig. S2.8).

To test these hypotheses, we dissected TlnB into its minimal PKS component of ACP_{cis} and SAT-KS-MAT⁰, in which the malonyl acyl transferase (MAT) domain is deactivated. Working with minimum PKS allowed us to achieve higher expression of the dissected proteins for assays (36), and provides a direct examination of the effects of ψ ACP on the extension step from tetraketide to pentaketide, after which pyrone 7 is the expected product. We performed a single-round chain extension assay in which the tetraketide 10 was used as a starter unit to prime the KS domain (Fig. 5A). Malonyl-ACP_{cis} was generated by preloading malonyl-CoA on apo-ACP_{cis} with NpgA. Using preloaded malonyl-ACP_{cis} together with SAT-KS-MAT⁰ can exclude any possible ψ ACP–MAT interactions in the assay. In the presence of an increasing amount of ψ ACP relative to SAT-KS-MAT⁰ and malonyl-ACP_{cis}, the yield of 7 significantly decreases (Fig. 5B),

confirming that ψ ACP can inhibit a chain extension event catalyzed by KS. We next compared the inhibitory activities of ψ ACP-MT on minimal PKS with apo-ACP_{cis} and a noncognate apo-ACP from the NRPKS CazM (15). Likewise, we isolated the chain extension event from tetraketide to pentaketide by using minimal PKS SAT-KS-MAT and ACP_{cis}, and used tetraketide 10 to prime the KS domain. Here, the MAT was kept active so that multiple turnovers could take place to accumulate pyrone 7. In contrast to the strong inhibition observed with ψ ACP-MT, titrating apo-ACP_{cis} or noncognate ACP to TlnB minimal PKS led to only a moderate decrease in the yield of 7 (Fig. 5C and SI Appendix, Fig. S2.11).

Based on the recent structure of CTB1, which is an NRPKS synthesizing *nor*-toralactone (39), we propose a model of TlnC ψ ACP-MT interacting with TlnB NRPKS (Fig. 5D). Similar to known ACPs, multiple negatively charged residues are distributed throughout the first half of the ψ ACP sequence. These charges were shown to mediate protein–protein interactions between ACP and the PKS core (38) (SI Appendix, Fig. S2.12). In our model, ψ ACP binds to the KS domain via similar electrostatic interactions and promotes departure of tetraketidyl-ACP_{cis} from the KS active site and methylation by TlnC; following methylation, methylated tetraketidyl-ACP_{cis} enters the KS domain for the next extension step. Previous findings showed that each catalytic step in IPKS machineries is a result of kinetic competition between functional domains (35, 40). Here, the dissociated nature of the TlnC MT has a lower effective concentration compared with its in-line counterparts (41). To compensate for the kinetic loss, a decoy ψ ACP is recruited to slow down KS-catalyzed chain elongation, while providing protein–protein interactions to facilitate TlnC MT functions.

Discussion

T. harzianum t-22, widely used as a biofertilizer and biocontrol fungus, utilizes small molecules to enable chemical communication with neighboring plants (11). Many of the *T. harzianum* t-22 biosynthetic clusters are silent under laboratory conditions, and are not associated with known natural products. We activated the transcription of a silent IPKS cluster of interest that led to the production of a pair of unique redox active molecules 1 and 2. Selection of the target cluster was driven by an intriguing collection of biosynthetic enzymes, including the tandem IPKSs and the ψ ACP-MT fusion protein. Production of the sorbyl-hydroquinone 1 was not anticipated a priori, and underscores the potential of using genome mining to find new natural products. Importantly, we showed 1 can readily reduce Fe(III) to Fe(II) under physiological conditions, and can help *A. thaliana* reductively assimilate Fe(III). Small diffusible molecules produced by *T. harzianum* t-22 were previously shown to reduce Fe(III) to Fe(II) (26), and 1 may therefore be one such molecule. Although the exact role of 1 in fungal host physiology is unknown, our work shows that identifying these compounds and elucidating their mechanisms can accelerate the development of new natural products in agriculture.

Our work here also unveiled unique programming features of fungal NRPKS. TlnC is an example in thiol template biosynthesis (PKS and NRPS) that an inactive ACP plays an important role. The nonphosphopantetheinylated nature of ψ ACP renders it incapable of shuttling polyketide intermediates and eliminates competition with ACP_{cis} for the TlnC active site. However, the intact ACP tertiary structure and conserved surface charge residues allow the apo-ACP to inhibit decarboxylative condensation, possibly through interacting with the KS domain. Such binding may hinder the re-entry of the tetraketide-ACP to the KS domain and allow it to be methylated by the MT domain.

The fused ψ ACP domain provides kinetic benefits to the methylation step. Methylation by Δ TlnC without the fused ψ ACP is less efficient, as shown by the product ratio of pyrone 7 and 3 (Fig. 4B, iii), which implies that the MT alone is not kinetically competent enough to compensate for its dissociation from NRPKS. In fact, it appears that TlnC methylation activity may be

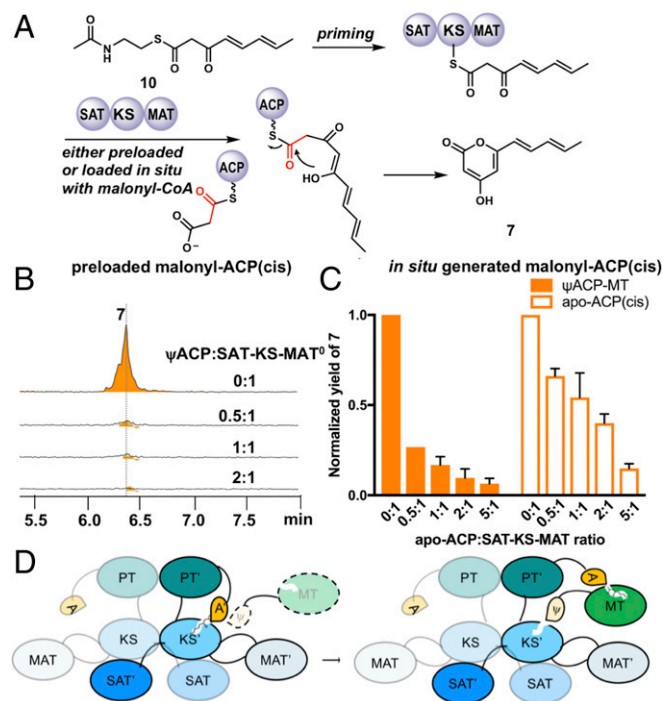


Fig. 5. ψ ACP inhibits KS to allow for methylation by TlnC *in trans*. (A) Minimum TlnB PKS primed with 10 leads to the formation of 7. (B) When using malonyl-ACP_{cis}, increasing the molar ratio of ψ ACP to SAT-KS-MAT⁰ decreases formation of 7. (C) Inhibition of minimal TlnB PKS by ψ ACP-MT is significant. (D) Proposed model of the role of ψ ACP in facilitating methylation of 3-oxo-4,6-octadienoyl ACP_{cis} by TlnC. PT, product template.

intrinsically slower compared with other in-line MTs. A recent study on citrinin PksCT shows that equimolar complementation of its in-line MT *in trans* almost completely restores the polyketide methylation pattern (40). The fusion of ψ ACP can establish protein–protein interactions between TlnC and NRPKS TlnB. As a result, the MT can be recruited to the NRPKS and minimize the exposure of the reactive poly- β -ketone chain to solvent.

The NRPKS machinery in the *tlh* cluster essentially has two ACPs, with one catalytically inactive but functionally essential. This is in contrast to NRPKSs, which use two catalytically active and functionally equivalent ACPs, as in the case of CTB1 and naphthopyrone synthase wA (39, 42). Such tandemly arranged *holo*-ACPs are synergetic in shuttling acyl intermediates into different functional domains to improve biosynthetic efficiency (43). Therefore, tandem *holo*-ACPs and ψ ACP may represent different time points during NRPKS evolution: Gene duplication yielded tandem ACPs in NRPKS, while later gene fission and mutation afforded ψ ACP the opportunity to play more of a structural and regulatory role (44, 45) (*SI Appendix*, Fig. S2.13). A genome survey of other sequenced fungi reveals that additional ψ ACP fusion to polyketide-modifying enzymes can be found in cryptic PKS gene clusters (*SI Appendix*, Fig. S2.14). These ψ ACP fusion enzymes may employ hitherto unknown programming rules in the biosynthesis of new natural products.

Conclusions

We discovered redox-active *o*-hydroquinone tricholignan A 1 from biofertilizer fungus *T. harzianum* t-22 via a genome mining approach. Tricholignan A can reduce Fe(III) to Fe(II), and may be among the molecules that are synthesized by *T. harzianum* t-22 in soil and help plants acquire Fe(II). Tricholignan A is synthesized by a tandem PKS pair, with the additional assistance of an unusual ψ ACP-MT fusion protein. The ψ ACP, which must be kept in *apo* form, is proposed to interact with the PKS to enhance access of the MT domain to the polyketide substrate. This study reveals unique natural products from fungi that benefit plant fitness, as well as unusual biosynthetic logic by IPKSs.

Materials and Methods

Analyses of fungal and yeast metabolic profiles and enzymatic reactions were monitored by liquid chromatography (LC)/MS with a Phenomenex Kinetex LC column. All enzymatic reactions were conducted at room temperature. Additional procedures are detailed in *SI Appendix*.

ACKNOWLEDGMENTS. We thank Dr. J. Clardy for providing *T. harzianum* t-22 strain and Dr. E. Sattely for providing *A. thaliana* *f6'h1* mutant seeds. We thank Dr. F. Liu for assistance with cyclic voltammetry and Drs. R. Giehl and Y. Hai for constructive discussion. This work was supported by NIH Grant 1R35GM118056 (to Y.T.) Chemical characterization studies were supported by shared instrumentation grants from the National Science Foundation (Grant CHE-1048804).

- Lorito M, Woo SL, Harman GE, Monte E (2010) Translational research on *Trichoderma*: From 'omics to the field. *Annu Rev Phytopathol* 48:395–417.
- Contreras-Cornejo HA, Macias-Rodríguez L, Cortés-Penagos C, López-Bucio J (2009) *Trichoderma virens*, a plant beneficial fungus, enhances biomass production and promotes lateral root growth through an auxin-dependent mechanism in Arabidopsis. *Plant Physiol* 149:1579–1592.
- Sivan A, Ucko O, Chet I (1987) Biological control of Fusarium crown rot of tomato by *Trichoderma harzianum* under field conditions. *Plant Dis* 71:587–592.
- Pusztahelyi T, Holb IJ, Pócsi I (2015) Secondary metabolites in fungus-plant interactions. *Front Plant Sci* 6:573.
- Stringlis IA, Zhang H, Pieterse CMJ, Bolton MD, de Jonge R (2018) Microbial small molecules—Weapons of plant subversion. *Nat Prod Rep* 35:410–433.
- Hart MM, et al. (2017) Fungal inoculants in the field: Is the reward greater than the risk? *Funct Ecol* 32:126–135.
- Brakhage AA (2013) Regulation of fungal secondary metabolism. *Nat Rev Microbiol* 11:21–32.
- Bergmann S, et al. (2007) Genomics-driven discovery of PKS-NRPS hybrid metabolites from *Aspergillus nidulans*. *Nat Chem Biol* 3:213–217.
- Sato M, et al. (2017) Collaborative biosynthesis of maleimide- and succinimide-containing natural products by fungal polyketide megasynthases. *J Am Chem Soc* 139:5317–5320.
- Harman GE (2000) Myths and dogmas of biocontrol changes in perceptions derived from research on *Trichoderma harzianum* t-22. *Plant Dis* 84:377–393.
- Contreras-Cornejo HA, Macias-Rodríguez L, del-Val E, Larsen J (2016) Ecological functions of *Trichoderma* spp. and their secondary metabolites in the rhizosphere: Interactions with plants. *FEMS Microbiol Ecol* 92:fiw036.
- Chooi YH, Tang Y (2012) Navigating the fungal polyketide chemical space: From genes to molecules. *J Org Chem* 77:9933–9953.
- Simpson TJ (2014) Fungal polyketide biosynthesis—A personal perspective. *Nat Prod Rep* 31:1247–1252.
- al Fahad A, et al. (2014) Oxidative dearomatization: The key step of sorbicillinoid biosynthesis. *Chem Sci* 5:523–527.
- Winter JM, et al. (2012) Identification and characterization of the chaetoviridin and chaetomugilin gene cluster in *Chaetomium globosum* reveal dual functions of an iterative highly-reducing polyketide synthase. *J Am Chem Soc* 134:17900–17903.
- Weber T, et al. (2015) antiSMASH 3.0—a comprehensive resource for the genome mining of biosynthetic gene clusters. *Nucleic Acids Res* 43:W237–43.
- Keating DH, Carey MR, Cronan JE, Jr (1995) The unmodified (*apo*) form of *Escherichia coli* acyl carrier protein is a potent inhibitor of cell growth. *J Biol Chem* 270:22229–22235.
- Flugel RS, Hwangbo Y, Lambalot RH, Cronan JE, Jr, Walsh CT (2000) Holo-(acyl carrier protein) synthase and phosphopantetheinyl transfer in *Escherichia coli*. *J Biol Chem* 275:959–968.
- Crawford JM, Vagstad AL, Ehrlich KC, Udvary DW, Townsend CA (2008) Acyl-carrier protein-phosphopantetheinyltransferase partnerships in fungal fatty acid synthases. *ChemBioChem* 9:1559–1563.
- Hlouchova K, Rudolph J, Pietari JM, Behlen LS, Copley SD (2012) Pentachlorophenol hydroxylase, a poorly functioning enzyme required for degradation of pentachlorophenol by *Sphingobium chlorophenolicum*. *Biochemistry* 51:3848–3860.
- Biedermann D, Vavříková E, Cvak L, Křen V (2014) Chemistry of silybin. *Nat Prod Rep* 31:1138–1157.
- Steenken S, Neta P (1982) One-electron redox potentials of phenols. Hydroxy- and aminophenols and related compounds of biological interest. *J Phys Chem* 86:3661–3667.
- Rajniak J, et al. (2018) Biosynthesis of redox-active metabolites in response to iron deficiency in plants. *Nat Chem Biol* 14:442–450.
- Kobayashi T, Nishizawa NK (2012) Iron uptake, translocation, and regulation in higher plants. *Annu Rev Plant Biol* 63:131–152.
- Spiller S, Terry N (1980) Limiting factors in photosynthesis: II. Iron stress diminishes photochemical capacity by reducing the number of photosynthetic units. *Plant Physiol* 65:121–125.
- Altomare C, Norvell WA, Bjorkman T, Harman GE (1999) Solubilization of phosphates and micronutrients by the plant-growth-promoting and biocontrol fungus *Trichoderma harzianum* rifai 1295-22. *Appl Environ Microbiol* 65:2926–2933.
- Zhang J, et al. (2016) The neutral metalloproteinase NMP1 of *Trichoderma guizhouense* is required for mycotrophy and self-defence. *Environ Microbiol* 18:580–597.
- Chirino-Valle I, et al. (2016) Potential of the beneficial fungus *Trichoderma* to enhance ecosystem-service provision in the biofuel grass *Miscanthus x giganteus* in agriculture. *Sci Rep* 6:25109.
- Hashimoto M, Nonaka T, Fujii I (2014) Fungal type III polyketide synthases. *Nat Prod Rep* 31:1306–1317.
- Ma SM, et al. (2009) Complete reconstitution of a highly reducing iterative polyketide synthase. *Science* 326:589–592.
- Suzuki K, Katagiri M (1981) Mechanism of salicylate hydroxylase-catalyzed decarboxylation. *Biochim Biophys Acta* 657:530–534.
- Huang Z, et al. (2015) A divergent and selective synthesis of *ortho*- and *para*-quinones from phenols. *Tetrahedron* 71:5871–5885.
- Crawford JM, Townsend CA (2010) New insights into the formation of fungal aromatic polyketides. *Nat Rev Microbiol* 8:879–889.
- Zhou H, Li Y, Tang Y (2010) Cyclization of aromatic polyketides from bacteria and fungi. *Nat Prod Rep* 27:839–868.
- Cacho RA, et al. (2015) Understanding programming of fungal iterative polyketide synthases: The biochemical basis for regioselectivity by the methyltransferase domain in the lovastatin megasynthase. *J Am Chem Soc* 137:15688–15691.
- Storm PA, Herbst DA, Maier T, Townsend CA (2017) Functional and structural analysis of programmed C-methylation in the biosynthesis of the fungal polyketide citrinin. *Cell Chem Biol* 24:316–325.
- Lee KK, Da Silva NA, Kealey JT (2009) Determination of the extent of phosphopantetheinylation of polyketide synthases expressed in *Escherichia coli* and *Saccharomyces cerevisiae*. *Anal Biochem* 394:75–80.
- Bruegger J, et al. (2013) Probing the selectivity and protein-protein interactions of a nonreducing fungal polyketide synthase using mechanism-based crosslinkers. *Chem Biol* 20:1135–1146, and erratum (2014) 21:913.
- Herbst DA, et al. (2018) The structural organization of substrate loading in iterative polyketide synthases. *Nat Chem Biol* 14:474–479.
- Storm PA, Pal P, Huitt-Roehl CR, Townsend CA (2018) Exploring fungal polyketide C-methylation through combinatorial domain swaps. *ACS Chem Biol* 13:3043–3048.
- Castellana M, et al. (2014) Enzyme clustering accelerates processing of intermediates through metabolic channeling. *Nat Biotechnol* 32:1011–1018.
- Fujii I, Watanabe A, Sankawa U, Ebizuka Y (2001) Identification of Claisen cyclase domain in fungal polyketide synthase WA, a naphthopyrone synthase of *Aspergillus nidulans*. *Chem Biol* 8:189–197.
- Gu L, et al. (2011) Tandem acyl carrier proteins in the curacin biosynthetic pathway promote consecutive multienzyme reactions with a synergistic effect. *Angew Chem Int Ed Engl* 50:2795–2798.
- Leonard G, Richards TA (2012) Genome-scale comparative analysis of gene fusions, gene fissions, and the fungal tree of life. *Proc Natl Acad Sci USA* 109:21402–21407.
- Pils B, Schultz J (2004) Inactive enzyme-homologues find new function in regulatory processes. *J Mol Biol* 340:399–404.

Supporting Information

Genome Mining and Biosynthesis of a Polyketide From a Biofertilizer Fungus that can Facilitate Reductive Iron Assimilation in Plant

Mengbin Chen^a, Qikun Liu^{b,c}, Shu-Shan Gao^a, Abbegayle E. Young^a, Steve E. Jacobsen^{b,c}, Yi Tang^{a,d,1}

^aDepartment of Chemical and Biomolecular Engineering, ^bDepartment of Molecular Cell and Developmental Biology, ^cHoward Hughes Medical Institute, ^dDepartment of Chemistry and Biochemistry, University of California, Los Angeles, California 90095, United States

¹ Email: yitang@g.ucla.edu

Table of Contents

1. Materials and Methods.....	4
1.1. Fungal genetics and culturing.....	4
1.2. Plasmid construction	4
1.3. Compound identification, isolation, and characterization	4
1.4. Reconstitution of tricholignan pathway in yeast.....	5
1.5. Protein expression and purification.....	5
1.6. Enzymatic assays	6
1.7. Cyclic voltammetry	7
1.8. Iron reduction kinetics assays	7
1.9. Circular dichroism (CD).....	8
1.10. Plant phenotypic characterization on agar plates.....	8
2. Supporting figures.....	9
2.1. RT-PCR analysis of <i>Tln</i> cluster	9
2.2. Structures of compounds 4, 4', and 5.....	10
2.3. Cyclic voltammetry	11
2.4. Iron reduction by tricholignan 1 <i>in vitro</i> at various pH.	12
2.5. <i>tln</i> cluster is highly conserved in several plant-beneficial <i>Trichoderma</i> spp.	13
2.6. The catalytic sequences of TlnE and TlnF.....	14
2.7. Determining the product profile of TlnA by <i>in vitro</i> reaction.....	15
2.8. Increasing the ratio of ψ ACP to Δ TlnC moderately rescued the production percentage of 3	16
2.9. MALDI-TOF analysis of ACPs.....	17
2.10. CD spectra of ψ ACP and ACP _{cis}	18
2.11. Non-cognate ACP moderately inhibits ketide extension by minimal PKS SAT-KS-MAT	19
2.12. Multiple sequence alignment of previously reported ACPs from NRPKS	20
2.13. A Proposed evolution route to ψ ACP-MT	21
2.14. Compilation of clusters with pseudo-ACP fusion proteins.....	22
2.15. SDS-PAGE analysis.....	23
2.16. UV and MS spectra of compounds characterized in this study	25
3. Tables.....	30
Table S1. Primers used in this study.....	30
Table S2. Deduced functions of <i>tln</i> cluster genes.	33
Table S3. Plasmids used for protein expression in this study.....	34
Table S4. ¹ H (500 MHz) and ¹³ C (125 MHz) NMR data of 2 in CD ₃ OD.....	35
Table S5. ¹ H (500 MHz) and ¹³ C (125 MHz) NMR data of 3 in CD ₃ OD.....	36

Table S6. ^1H (500 MHz) and ^{13}C (125 MHz) NMR data of 4 in CD_3OD	37
Table S7. ^1H (500 MHz) and ^{13}C (125 MHz) NMR data of 5 in CD_3OD	38
Table S8. ^1H (500 MHz) and ^{13}C (125 MHz) NMR data of 4' in CD_3OD	39
NMR spectra of compounds characterized in this study.....	40
^1H NMR spectrum of 2 in CD_3OD (500 MHz).	40
^{13}C NMR spectrum of 2 in CD_3OD (125 MHz).	40
HSQC spectrum of 2 in CD_3OD (500 MHz).	41
HMBC spectrum of 2 in CD_3OD (500 MHz).	41
COSY spectrum of 2 in CD_3OD (500 MHz).	42
^1H NMR spectrum of 3 in CD_3OD (500 MHz).	43
^{13}C NMR spectrum of 3 in CD_3OD (125 MHz).	43
HSQC spectrum of 3 in CD_3OD (500 MHz).	44
COSY spectrum of 3 in CD_3OD (500 MHz).	44
HMBC spectrum of 3 in CD_3OD (500 MHz).	45
^1H NMR spectrum of 4 in CD_3OD (500 MHz).	46
^{13}C NMR spectrum of 4 in CD_3OD (125 MHz).	46
COSY spectrum of 4 in CD_3OD (500 MHz).	47
HSQC spectrum of 4 in CD_3OD (500 MHz).	47
HMBC spectrum of 4 in CD_3OD (500 MHz).	48
NOESY spectrum of 4 in CD_3OD (500 MHz).	48
TROSY spectrum of 4 in CD_3OD (500 MHz).	49
^1H spectrum of 4' in CD_3OD (500 MHz).	50
^{13}C spectrum of 4' in CD_3OD (125 MHz).	50
COSY spectrum of 4' in CD_3OD (500 MHz).	51
HSQC spectrum of 4' in CD_3OD (500 MHz).	51
HMBC spectrum of 4' in CD_3OD (500 MHz).	52
NOESY spectrum of 4' in CD_3OD (500 MHz).	52
^1H spectrum of 5 in CD_3OD (500 MHz).	53
^{13}C spectrum of 5 in CD_3OD (125 MHz).	53
COSY spectrum of 5 in CD_3OD (500 MHz).	54
HSQC spectrum of 5 in CD_3OD (500 MHz).	54
HMBC spectrum of 5 in CD_3OD (500 MHz).	55
TROSY spectrum of 5 in CD_3OD (500 MHz).	55

1. Materials and Methods

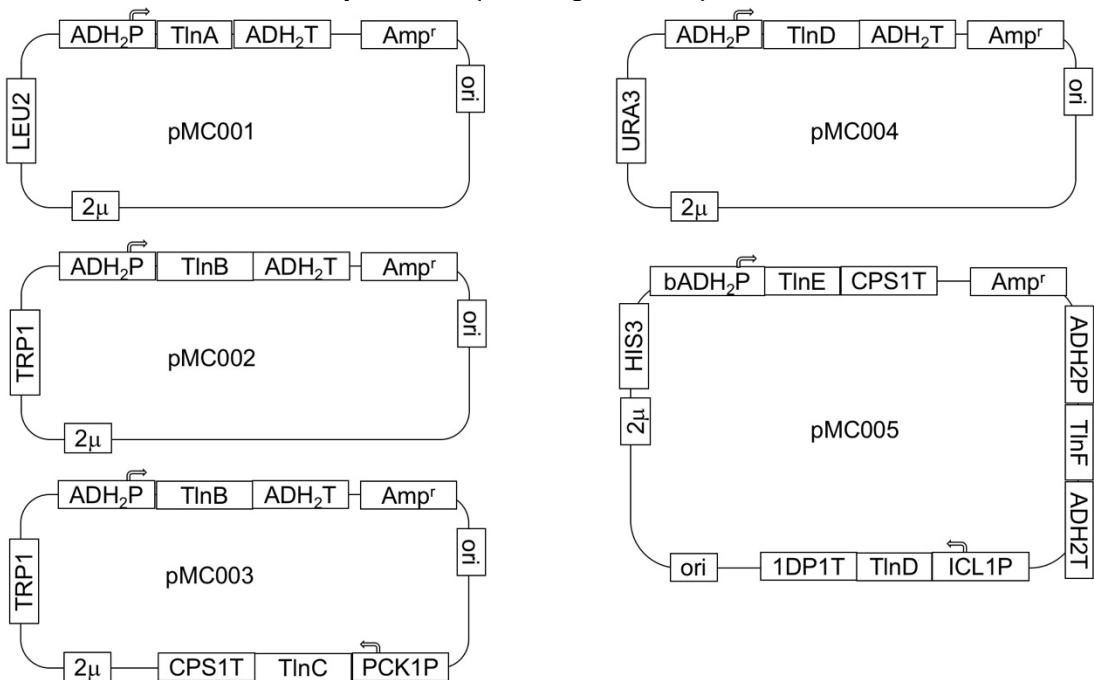
1.1. Fungal genetics and culturing

Trichoderma harzianum t-22 was cultivated in potato dextrose broth (PDB, sigma-aldrich) at 28 °C with aeration for 5-6 days. Genomic DNA extraction was carried out following the instructions of Zymo Quick-DNA Fungal/Bacterial Miniprep Kit. Spores were collected from a potato dextrose agar (PDA) plate grown at 28 °C for 4-5 days. For in-cluster transcription factor activation, PDA supplemented with 1.2 M sorbitol and 100 µg/mL hygromycin was used for protoplast regeneration and transformant selection (1).

After hygromycin-resistant transformants were obtained, first-round selection of transformants by metabolism profiling led to the identification of a transformant with new peaks of highest yields among all. This transformant, namely *T.harzianum* t-22*, was subject to further examination. After 2-day cultivation in PDB at 28 °C with aeration, the fungal bodies were collected and used for RNA extraction by Invitrogen RiboPure RNA purification Kit. RNA sample was then treated with DNase, followed by cDNA reverse transcription with Invitrogen SuperScript IV. Genes in the cluster of interest were amplified from cDNA by PCR using the primers in Table S1.

1.2. Plasmid construction

Plasmids used for yeast reconstitution and protein expression were constructed by amplifying corresponding open reading frames from cDNA reverse transcribed from cluster-activated fungal strain. The corresponding overlapping fragments were ligated to double-digested vectors, XW02, XW06, XW55, and JBH2B4, by yeast homologous recombination. Plasmids were confirmed by DNA sequencing, and maps were shown below.



1.3. Compound identification, isolation, and characterization

Small-scale compound production from *T.harzianum* TLB2 was performed in 50 mL falcon tubes containing 10 mL PDB. Dried residue from fungal bodies and supernatant was re-dissolved in 100 µL methanol, and applied to LC-MS analyses. Small-scale compound production from *Saccharomyces cerevisiae* BJ5464-NpgA was carried out in 15 mL glass tube

containing 2.5 mL YPD (2% dextrose). Supernatant was separated from cell pellet via centrifugation, and was extracted with ethyl acetate containing 1% acetic acid twice. Organic layer was dried *in vacuo* and residue was resuspended in 100 μ L methanol, and was applied to LC-MS analyses. All LC-MS analyses were performed on a Shimadzu 2020 EVLC-MS system (Phenomenex Kinetex, 1.7 μ m, 2.1 x 100 mm, C18 column) using positive and negative mode electrospray ionization at a flow rate of 0.3 mL/min using the gradient below of solvents A (0.1% formic acid in water) and B (0.1% formic acid in acetonitrile): holding 5% B for 0.25 min, followed by a 13-min linear gradient of 5-95%, and finished with holding at 95% for 4.75 min.

For large-scale compound purification, *T.harzianum* TLB2 was grown in 4-liter PDB at 28 °C with aeration for 4-5 days. Fungal bodies were separated from supernatant by filtering with miracloth (Millipore). Supernatant was extracted with ethyl acetate (3x), fungal bodies, on the other hand, were processed with acetone. Crude residue was dried under reduced pressure to yield an oil, and purified by silica gel column chromatography (1:1 hexane/ethyl acetate v/v). Fractions containing compounds of interest were combined and dried, respectively. Residue was re-dissolved in methanol and applied to preparative HPLC using a Shimadzu UFLC system and a COSMOSIL column (Nacalai Tesque Inc., 5C18-AR-II, 20ID x 250mm, flow rate of 8mL/min of solvents A (0.1% formic acid in water) and B (0.1% formic acid in acetonitrile): linear increase from 73% to 88%). Fractions that require further purification were subjected to HPLC chromatography with a Phenomenex Kinetex column: **2** and **9** with an isocratic wash of 39% acetonitrile in water supplemented with 0.1% formic acid, **4**, **5**, and **6** with an isocratic wash of 66% acetonitrile in water supplemented with 0.1% formic acid. **3** was purified with a COSMOSIL column (5C18-AR-II, 10ID x 250mm, flow rate of 4mL/min of solvents A (0.1% formic acid in water) and B (0.1% formic acid in acetonitrile): linear increase from 38% to 44%.

Off-pathway shunt product **8** was isolated from yeast harboring genes *TlnA*, *TlnB*, and *TlnD*. Supernatant of 4-liter yeast culture was separated from pellet by centrifugation, and was passed through XAD resin. Fraction containing **8** was eluted between 50% and 70% methanol in water, and was applied to a COSMOSIL column eluted with a gradient of 30-45% acetonitrile in water supplemented with 0.1% formic acid. Fractions containing **8** was dried *in vacuo*, and was further applied to a Phenomenex Kinetex column with an isocratic wash of 35% acetonitrile in water supplemented with 0.1% formic acid.

NMR spectra were acquired on a Bruker AV500 spectrometer with a 5 mm dual cryoprobe (^1H 500 MHz, ^{13}C 125 MHz).

1.4. Reconstitution of tricholignan pathway in yeast

Saccharomyces cerevisiae BJ5464-NpgA was transformed with corresponding plasmid combinations and was grown on select nutrient drop-out SD plates at 28 °C for 3 days. Single colony was picked up and grown in 2 mL SD media with selective nutrients dropped out for 1.5 days. 0.5 mL of SD media was then transferred to 2 mL YPD (2% dextrose) in a glass tube. The culture was shaken at 250 rpm at 28 °C for 2-3 days, target compounds are detectable after 48 hrs.

1.5. Protein expression and purification

1.5.1. Expression of *TlnA*, *TlnB*, and *TlnD*

TlnA, *TlnB*, and *TlnD* were expressed in *Saccharomyces cerevisiae* BJ5464-NpgA, respectively (2). *TlnA* gene was inserted into XW55 vector with N-terminal FLAG tag and C-terminal hexa-histidine tag. Genes of *TlnB* and *TlnD* were inserted into XW55 vector with C-terminal octa-histidine tag, respectively. Each plasmid was transformed into BJ5464-NpgA with Frozen E-Z Yeast Transformation Kit (Zymo) selected by uracil dropout media. Single colony was picked up from the plate and grown in 2.5 mL SD uracil-dropout media for 1 day, which was used to inoculate 500 mL SD uracil-dropout media and continued to grow 1.5 days. The culture

was equally split into 4 portions, each 125 mL was inoculated into 875 mL YPD media in shake flasks, and grown at 28 °C for 3 days with aeration. Cells were pelleted and stored at 80 °C.

Protein obtained from *S. cerevisiae* BJ5464-NpgA was purified following the general procedure: every 10 grams of cell pellet was resuspended in 20 mL buffer K (100 mM K₂HPO₄, 100 mM NaCl, pH 7.8). Cell suspension was lysed by blending and sonication, followed by clarification via high-speed centrifugation. The supernatant was incubated with Ni-NTA resin overnight, and the mix was applied to a column for wash and elution with gradually increasing concentrations of imidazole in buffer K. Most active fractions determined by SDS-PAGE gel were combined and concentrated by Amicon concentrators (Millipore), and protein concentrations were determined by Bradford assay.

1.5.2. Expression of TlnC and truncated variants of TlnB

E. coli BL21(DE3) was transformed with *N*-terminal His tagged TlnC, minimum PKS variants of TlnB, TlnE, TlnF, and ACPs, respectively, all with a TEV cleavage site. *E. coli* colonies were inoculated into 5X5 mL LB Miller Broth supplemented with 50-100 µg/mL antibiotics to provide selection pressure, which were grown overnight at 37 °C. These overnight inoculums were then added into 5 1-liter LB Miller Broth containing 50 µg/mL kanamycin. The cultures were grown at 37 °C until OD₆₀₀ reached 0.8, and were cooled to 16 °C. 0.07-0.1 mM IPTG was added into the culture, and protein expression lasted for 16-20 hrs. Cells were pelleted by centrifuging at 5,300 rpm for 15 minutes, and were stored at -80 °C for downstream characterization.

Protein purification follows the general procedure: every 10 grams of cell pellet was resuspended in 20 mL buffer A (50 mM Tris and 200 mM NaCl, pH 7.8). Cells were lysed by sonication and subsequently clarified by centrifugation. The supernatant was incubated with Ni-NTA resin overnight. The slurry was loaded onto a column, washed, and eluted with increasing concentrations of imidazole in buffer A. The fractions were examined by SDS-PAGE gels, most active fractions were combined and concentrated by Amicon concentrators (Millipore). The concentrated protein samples were buffer-exchanged into buffer containing 50 mM HEPES (pH 7.2), 200 mM NaCl, and 5% glycerol, and stored at -80 °C.

As for truncated variants of TlnB, we found that activities of His-tagged proteins were undetectable. In contrast, once these truncated variants were tag-free, they became highly active. Therefore, slight adjustment to accommodate for an extra step of TEV protease cleavage was made for truncated variants of TlnB. Eluate from Ni column was incubated with His-tagged Tobacco Etch Virus (TEV) protease overnight at 4 °C and dialyzed against dialysis buffer (50 mM Tris, 300 mM NaCl, 5% glycerol, pH 8.1). Next, the protein mixture was mixed with Ni resin and incubated at 4 °C for 3-5 hrs. The slurry was applied to an empty column, and washed with buffer B (50 mM Tris and 350 mM NaCl, pH 8.2), buffer B containing 20 mM imidazole, and eluted with buffer B containing 200 mM imidazole. SDS-PAGE gel confirmed that the presence of truncated variants of TlnB in flow-through and low-imidazole-concentration wash fractions. These two fractions were combined and concentrated, and buffer exchanged into 100 mM HEPES (pH 7.2) for assays by Zeba-Spin columns (ThermoFisher).

1.6. Enzymatic assays

ACPs purified from *E. coli* are all in *apo* form, as determined by MALDI-TOF. To convert them into *holo* form, 125 µM *Aspergillus nidulans* phosphopantetheinyl(ppant) transferase NpgA was incubated with 10 mM MgCl₂, 1 mM CoA, and 100 µM *apo*-ACPs of interest for 1 hour at room temperature (3). According to MALDI-TOF results, conversion was completed under such conditions.

A single turnover reaction of TlnA *in vitro* contained 6.5 mM NADPH (CALZYME), 4.5 mM malonyl-CoA (CoALA Biosciences), and 49 μ M TlnA in 100 mM HEPES (pH 7.2). One fifth total reaction volume of 1N NaOH was added into the overnight reaction mixture to quench the reaction, followed by heat treatment at 65 °C for 12 minutes. The mixture was then extracted with 250 μ L ethyl acetate (1% acetic acid) twice, and the top layers were combined and dried by speedvac. Residue was re-suspended in methanol and clarified by centrifugation. The supernatant was loaded onto LC-MS for analysis. Enzymatic reaction product was compared with 2,4-hexadienoic acid standard obtained from Acros Organics.

In vitro activity assays with variants of TlnC: equimolar (in the range of 20-30 μ M) TlnA, TlnB, TlnC, and TlnD were mixed, with 5 mM NADPH, 5 mM malonyl-CoA, and 10 mM S-adenosyl methionine (SAM, Sigma-Aldrich) in 100 mM HEPES (pH 7.2). Reaction progressed overnight at room temperature, and was terminated by adding one fifth total reaction volume of 1N NaOH. The mixture was incubated at 65 °C for 12 minutes, and was subsequently extracted with 250 μ L ethyl acetate (1% acetic acid) twice. The organic layers were combined and transferred to a new tube to be dried by speedvac. Residue was dissolved in methanol and clarified by centrifugation, and the supernatant was applied to LC-MS for analysis.

Titration assays of TlnB with ψ ACP: 16 μ M of TlnA, TlnB, Δ TlnC, and TlnD were incubated with increasing molar ratios of ψ ACP (1:1, 2:1, 4:1, and 7:1) overnight, in the presence of 4 mM NADPH, 7.6 mM SAM, and 3.2 mM malonyl-CoA in 100 mM HEPES (pH 7.2). Polyketide products were extracted as aforementioned, and were quantified by calculating MS peak area, with the assumption that ionization efficiency of **3** and **7** are equivalent.

Titration assays of minimum PKS SAT-KS-MAT with ACPs or TlnC: equimolar (in the range of 16-36 μ M) SAT-KS-MAT and TlnD were incubated overnight with increasing molar ratios of ACPs or TlnC (0:1, 0.5:1, 1:1, 2:1, and 5:1), in the presence of 1.25 mM corresponding SNAC substrate **10** and 2.4 mM malonyl-CoA in 100 mM HEPES (pH 7.2). Polyketide products were extracted as aforementioned, and were quantified by calculating UV peak area.

1.7. Cyclic voltammetry

Prior to measurements, buffers were degassed by sparging with N₂ gas overnight and were transferred to a glove box. Electrochemical experiment was carried out with a WaveDriver 20 Potentiostat (Pine Research) and a standard three-electrode configuration: an extensively-polished glassy carbon electrode as the working electrode, a carbon counter electrode, in the presence of an Ag|AgCl reference electrode (saturated KCl). 0.065 mM **2** was dissolved in 50 mM degassed sodium phosphate buffer at pH 6.4 and pH 7.0, respectively, with 5% acetonitrile (v/v) to improve solubility. Scans were carried out and duplicated in a glove box at 25 °C, with a scan rate of 0.1V/s. Redox potential of **2** was calculated by correcting the experimental value (+0.200 V) with a comparison to a normal hydrogen electrode, and further corrected with for pH (59 mV per pH unit). This yielded values versus the standard hydrogen electrode (pH 0).

1.8. Iron reduction kinetics assays

Assays were conducted in Britton-Robinson (BR) buffer at 4 different pHs, which were prepared as described previously (4). Reduction assays were run in a 96-well plate, containing 800 μ M FeCl₃, 2 mM ferrozine, and 25 μ M **1**. Negative control was conducted without adding **1**. After **1** was added to the assay mix, newly-formed Fe(II) complexes with ferrozine, and the absorbance at 562nm corresponding to the Fe(II)-ferrozine complex was used to monitor the progress.

1.9. Circular dichroism (CD)

CD spectra of ACPs were obtained on a JASCO J-715 Circular Dichroism spectrophotometer at room temperature using a 0.1 cm quartz cell. Protein samples were buffer exchanged to 10 mM sodium phosphate buffer (pH 7.0) and their concentrations were determined by absorbance at 280 nm prior to CD measurements. Spectra were obtained with a wavelength range from 260 nm to 190 nm, with an accumulation of 6.

1.10. Plant phenotypic characterization on agar plates

Seeds were sterilized as follows: 1) shaken in 1 mL 70% (v/v) ethanol containing 0.1% Triton X-100 for 15 minutes; 2) shaken in 1 mL 90% ethanol for 10 minutes. They were subsequently sown on plates containing full-strength Murashige and Skoog (MS) medium supplemented with 0.5% sucrose and 25 mM MES (pH 5.6). The medium was solidified with 1% agar. Seeds were stratified on agar for 2 days at 4 °C, and then transferred to growth cabinets. After 8 days, seedlings were transferred to new agar plates containing full-strength Fe-deficient MS medium with 20 μM FeCl₃, supplemented with 0.5% sucrose and 25 mM MES (pH 5.6), for 1-day starvation. Next, seedlings were transferred to full-strength Fe-deficient MS medium with 20 μM Fe-EDTA, supplemented with 0.5% sucrose, 25 mM MES (pH 5.6), and 150 μM tricholignan A. Equivalent amounts of methanol and EDTA were used as negative control and positive control, respectively. After 6-day growth, leaf disks were harvested for chlorophyll concentration determination. Briefly, leaf disks were bathed in dimethyl formamide (DMF) at 4 °C for 2 days. Absorbances at 647nm and 664 nm of DMF leaf extracts were measured by a UV-vis spectrophotometer (5). Experiments were repeated twice, and similar results were obtained.

2. Supporting figures

2.1. RT-PCR analysis of *Tln* cluster

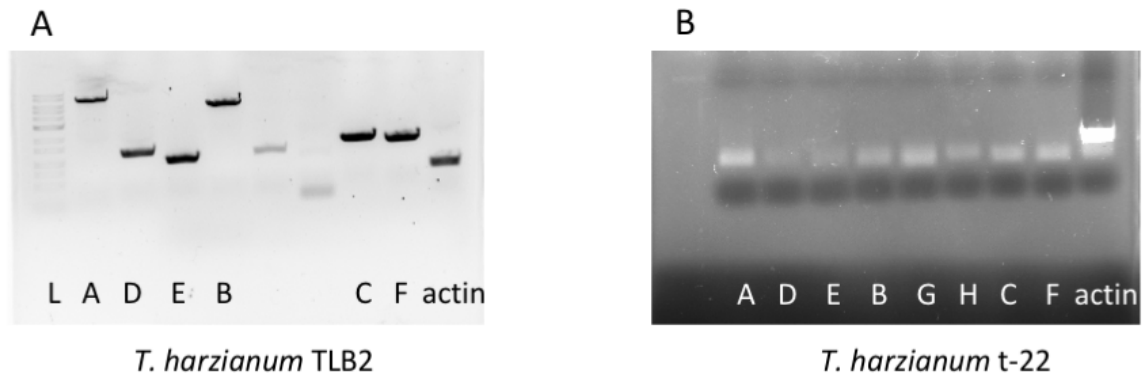


Fig. S2.1. RT-PCR analysis of *tln* cluster in (A) TF-activated strain and *T. harzianum* TLB2 and (B) wildtype *T. harzianum* t-22. L: 1 kb ladder (Lamda Biotech); A through F: genes in the *Tln* cluster; actin was used as a positive control.

2.2. Structures of compounds 4, 4', and 5.

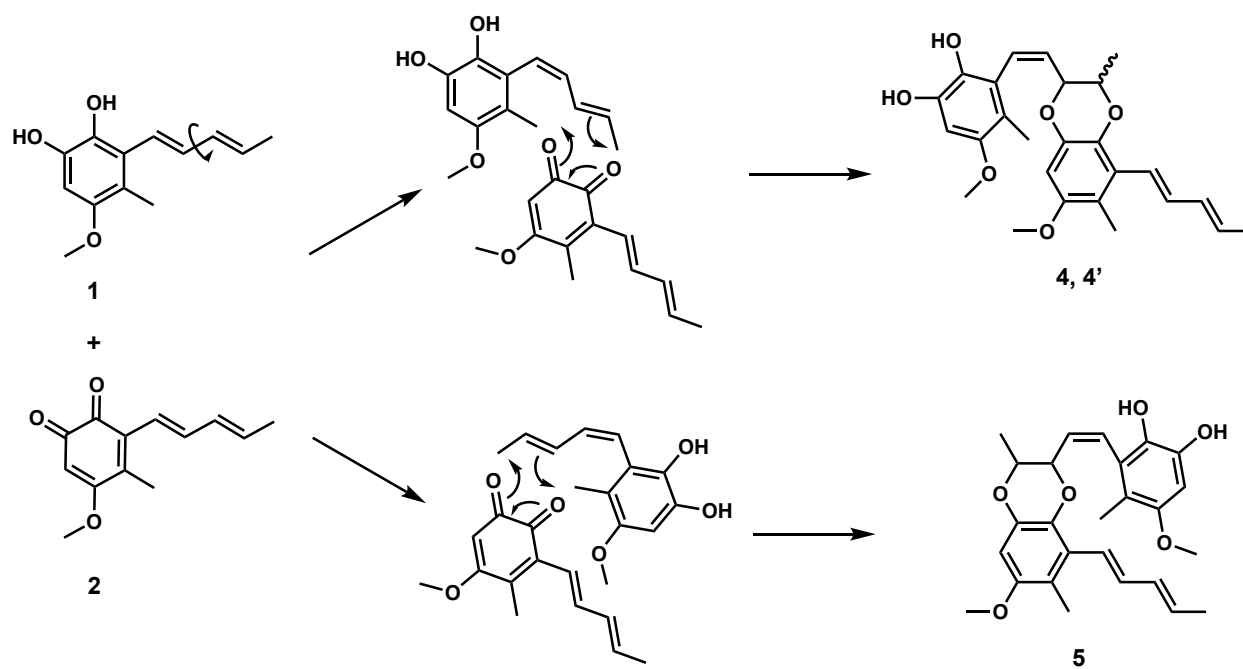
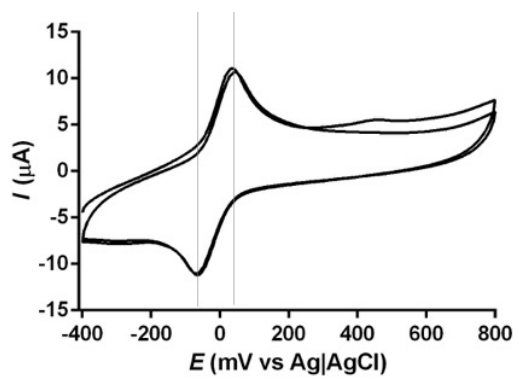


Fig. S2.2. Structures of 4, 4', and 5, which are likely derived from non-specific cycloadditions of 1 and 2.

2.3. Cyclic voltammetry

A



B

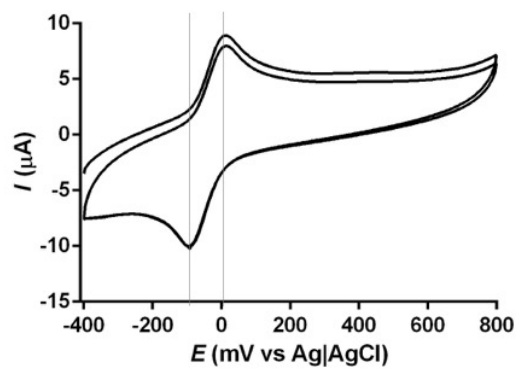


Fig. S2.3. Cyclic voltammetry traces of **2** at (A) pH 6.4 and (B) pH 7.0 obtained in aqueous phosphate buffer.

2.4. Iron reduction by tricholignan 1 *in vitro* at various pH.

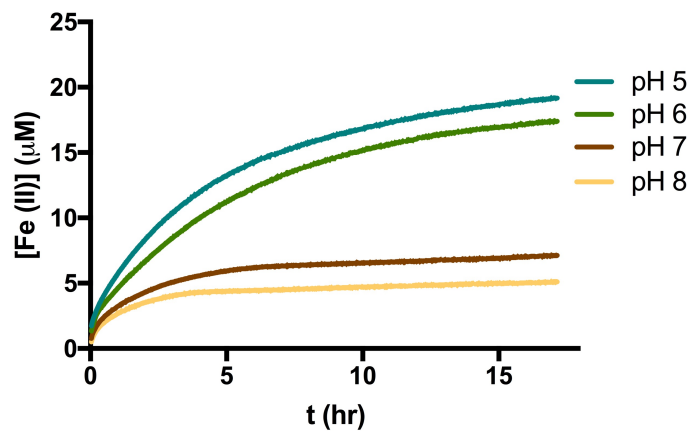


Fig. S2.4. Fe(III) reduction by 1 at various pH.

2.5. *tln* cluster is highly conserved in several plant-beneficial *Trichoderma* spp.

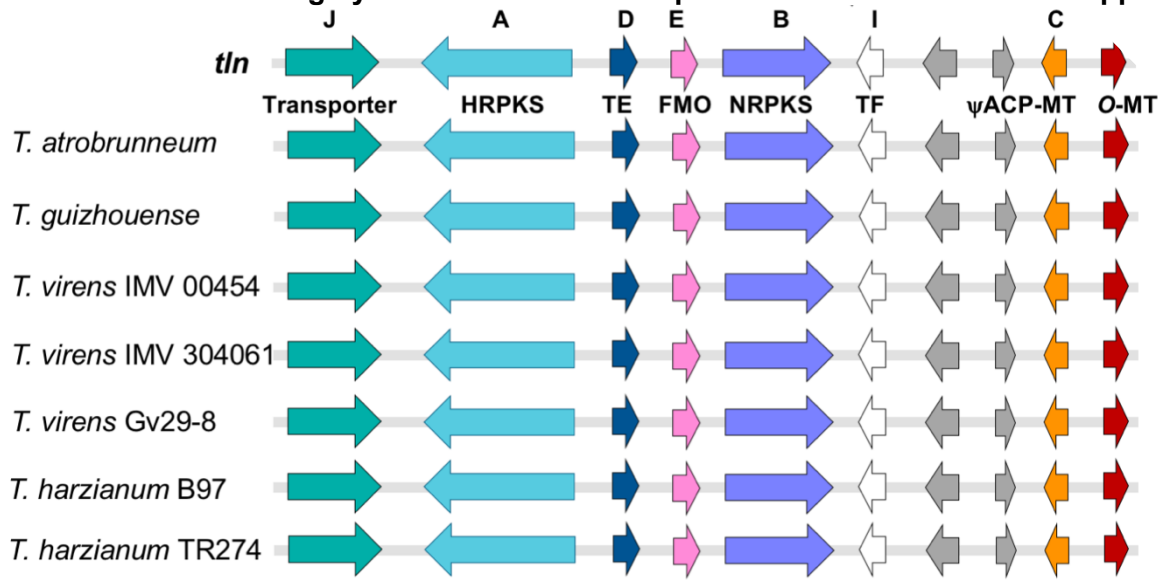


Fig. S2.5. *tln* cluster homologues can be found in other plant-beneficial *Trichoderma* spp, indicating their likely role in promoting plant fitness.

2.6. The catalytic sequences of TlnE and TlnF.

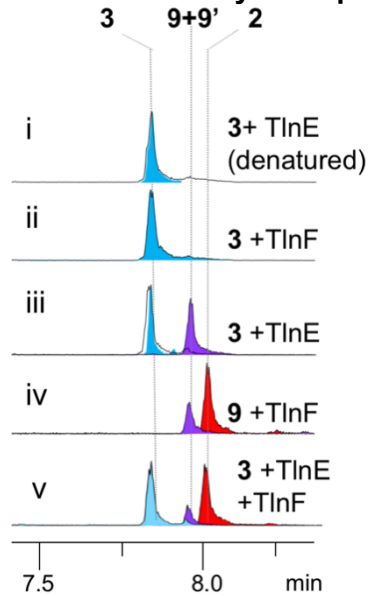


Fig. S2.6. Enzymatic reactions *in vitro* established the catalytic sequences of TlnE and TlnF.

2.7. Determining the product profile of TlnA by *in vitro* reaction.

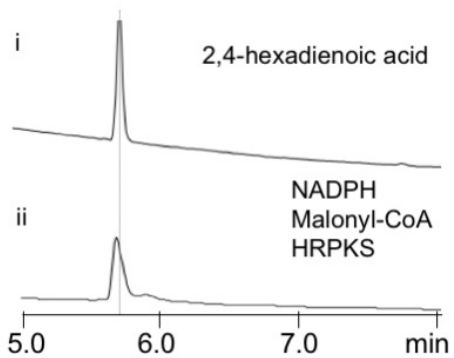


Fig. S2.7. UV traces of enzymatic reaction product of TlnA and comparison with the standard. TlnA, HRPKS in the cluster, provides 2,4-hexadienoyl group to be transferred to TlnB. The acid form of the intermediate can be detected by LC after basis hydrolysis and subsequent extraction of the enzymatic reaction with ethyl acetate containing 1% acetic acid.

2.8. Increasing the ratio of ψ ACP to Δ TlnC moderately rescued the production percentage of **3**

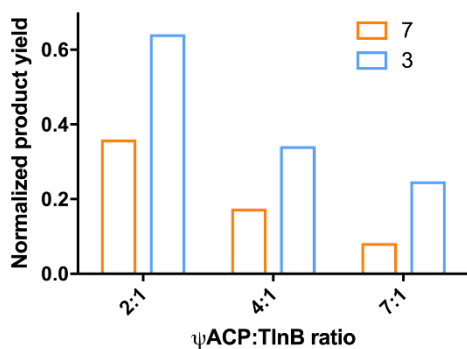


Fig. S2.8. Polyketides product distribution from the *in vitro* assays with ψ ACP titrated into the equimolar mix of TlnA, TlnB, Δ TlnC, and TlnD. We varied the ratio of the standalone ψ ACP and Δ TlnC in the reactions to determine how product distribution is affected. Increasing the ratio of ψ ACP to Δ TlnC restored the production of the methylated product **3**, but lowered total polyketide yield. Total polyketide yield (**3+7**) of the assay where the ratio of ψ ACP:TlnB is 2:1 is normalized to 1.

2.9. MALDI-TOF analysis of ACPs

ACP	<i>Apo</i> -form		<i>Holo</i> -form	
	Theoretical [M+Na] ⁺	Experimental [M+Na] ⁺	Theoretical [M+Na] ⁺	Experimental [M+Na] ⁺
TlnBACP _{cis}	12361	12362	12702	12702
ψACP	12755	12754	\	\
T34SψACP	12740	12740	13080	13079
ACP _{CM}	11851	11851	12191	12191

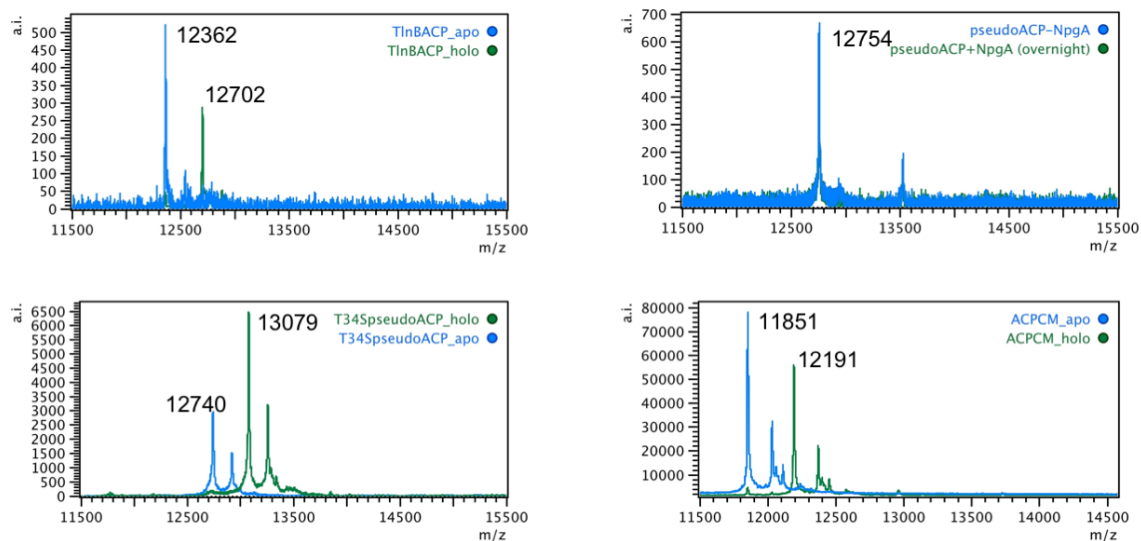


Fig. S2.9. MALDI-TOF analysis of ACPs used in this study. Plots in blue represent apo-ACPs, green ones represent ACPs incubated with NpgA and CoA. Ppant modification leads to a mass increase of 340 ± 1 Da, which applies to TlnBACP, T34SψACP, and ACP_{CM}. As for ψACP, the mass peak is not migrated after NpgA incubation, due to its incapability to be Ppant-modified. The additional mass of 178 Da in some spectra is caused by dephosphorylation of α-N-6-phosphogluconoylation of N-terminal His-tagged proteins.

2.10. CD spectra of ψ ACP and ACP_{cis}.

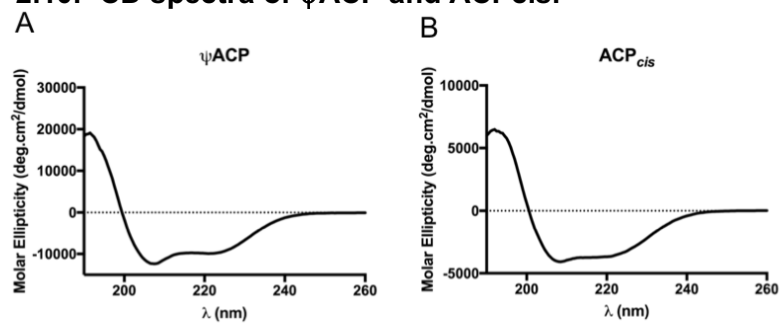


Fig. S2.10. Comparison of CD spectra of ψ ACP and ACP_{cis} revealed that ψ ACP adopts the characteristic α -helical folding observed among ACPs.

2.11. Non-cognate ACP moderately inhibits ketide extension by minimal PKS SAT-KS-MAT

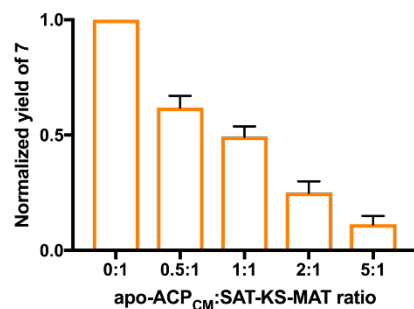


Fig. S2.11. Increasing molar ratios of non-cognate apo-ACP_{CM} to minimal PKS SAT-KS-MAT and ACP_{cis} moderately inhibits ketide extension, leading to a decrease of the formation of pyrone **7**. Tetraketide SNAC **10** was used as the substrate.

2.12. Multiple sequence alignment of previously reported ACPs from NRPKS

A

```

                1   10   20   30
ACPtrans      .....MSLEKVRETFCDVTGLDADEVEEDSELDELGVDTIIAKE
CazM_acp_1754-1828 .....RDITTEVRNLVAVHVSGLIEASEIGLDSEMADFGIDSLMGME
ACPcis        EPQASDDASASAGTKTPEASDLEIIDTLLSIVAREIGVNVDEMLDEAAFIDLGVDSLVAVT
PKSAacp       .....GSAPAAKGVGVSNKLDAMRVVSEESGIALEELTDDSNFADMGIDSLSSMV
CTB1_a        .....ALIAPALEIVSEETIRMPIDELKDDIDFTDAGLDSLLSLV
pks4_ACP      ..SVGTTSPPPEPTESPVGSASGLIQKALEIIADEIGVDISQLTDTLLADLGVDSLMSLT
CTB1_b        .....LTDPSP.....NEIGTVWRDALKILSEESGLTDEELTDDTSFADVGVDSLMSLV
  
```

```

                40   50   60   70   80   90
ACPtrans      LARKLSVFSGRAVES..SRILSENFIGLAHYIQSILDIGNDKETPSRK...QSHMEPT
CazM_acp_1754-1828 LGREVELTFKCKLDQ..AEQMEATSLRKFVAVVAKALFG.....
ACPcis        IFTTLEREVGLKLQA..SFFVEHTTVGNVKRALHEML.....
PKSAacp       IGSRFREDLGLDLGPEFSLFIDCTTVRAKDFMLGSGDAG.....
CTB1_a        ISSRMRDQLGIEFES..AQFMEIGSIGGLKEFLTR.....
pks4_ACP      ILGNFREELLDLIPAA..AQFYEFSTVQDLKSF LGANDQDFSSSNSEAESSASSAASTSPS
CTB1_b        ITSRLRDELLDLDFPD..RALFE.....
  
```

B



Fig. S2.12. (A) Multiple sequence alignment and (B) phylogenetic tree of NRPKS ACPs. The aspartate residue in DSL motif is highlighted in red, among all characterized ACPs, ψ ACP is the only one that has a threonine instead of serine (blue triangle pointed) for the potential Ppant installation site. Negatively-charged residues in ψ ACP are underlined in purple.

2.13. A Proposed evolution route to ψ ACP-MT

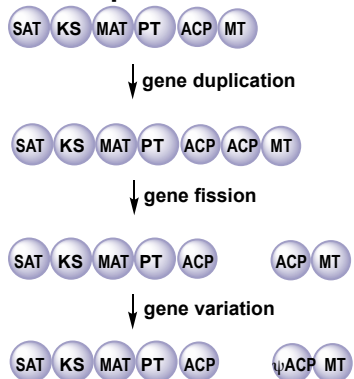
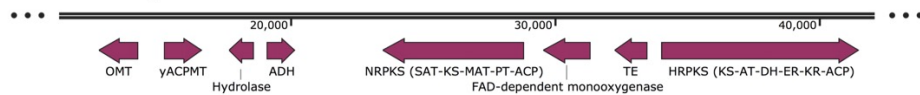


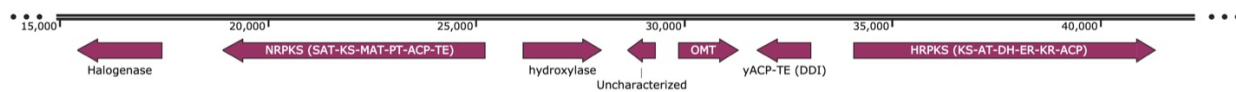
Fig. S2.13. A proposed evolution route to ψ ACP-MT from the canonical NRPKS domain architecture of SAT-KS-MAT-PT-ACP-MT. A gene duplication event is proposed to result in tandem ACPs; subsequent gene fission leads to two open reading frames of one biosynthetic machinery; over time, the second ACP becomes catalytically inactive and loses its original carrier protein function, but takes on a new regulatory role.

2.14. Compilation of clusters with pseudo-ACP fusion proteins

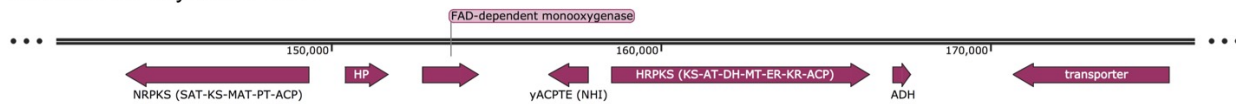
Trichoderma guizhouense



Talaromyces marneffei



Metarhizium rileyi RCEF 4871



Verruconis gallopava CBS 43764

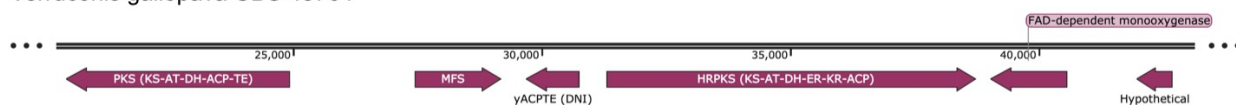
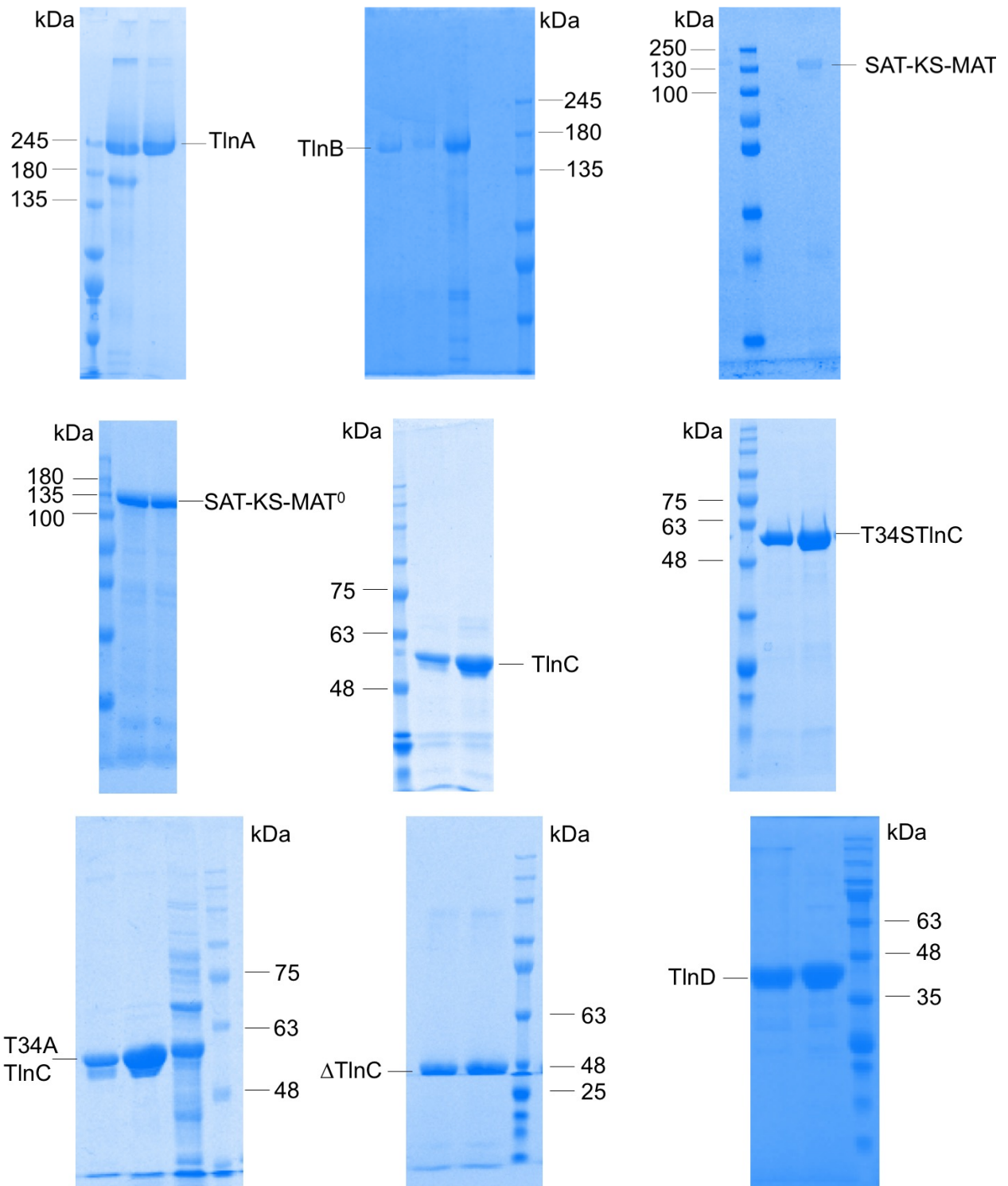
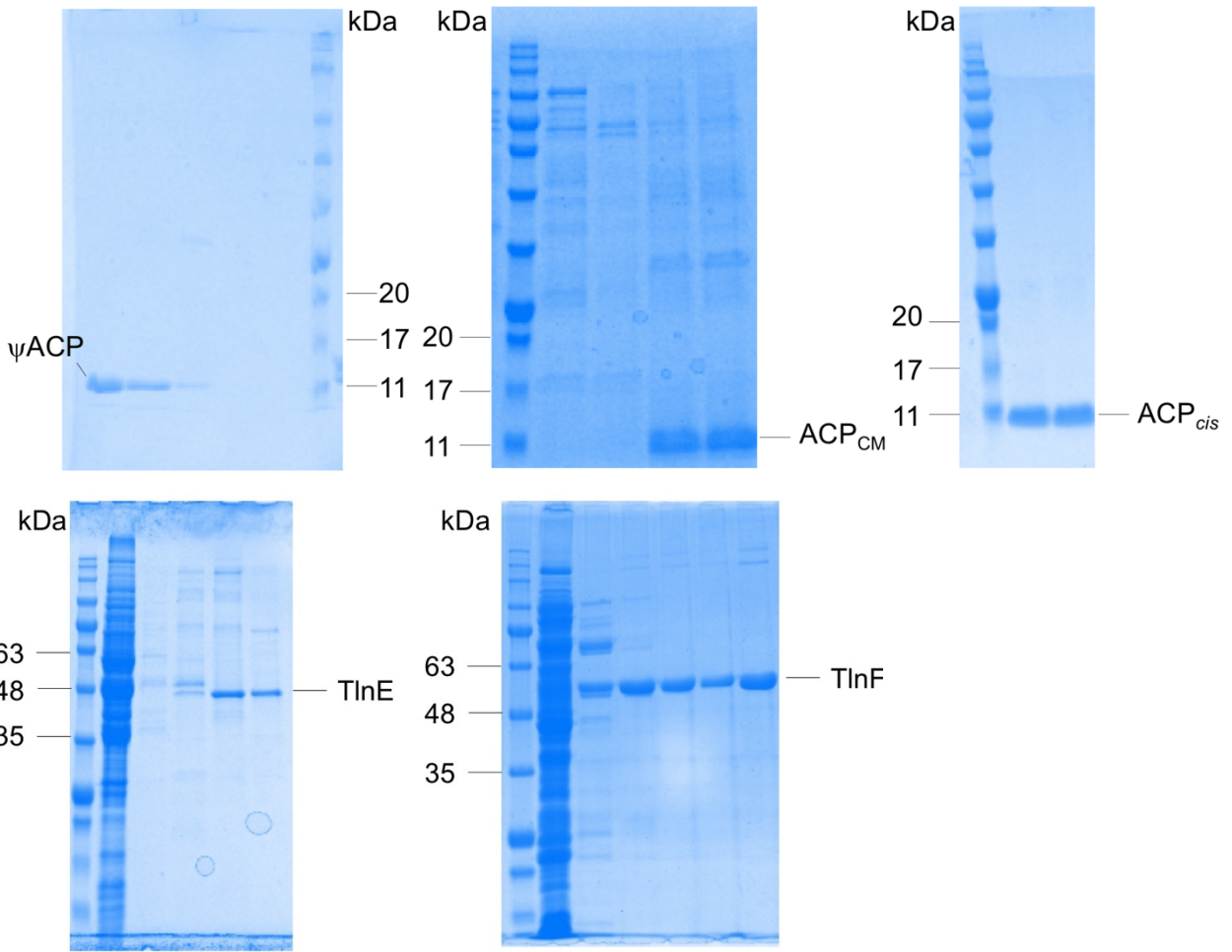


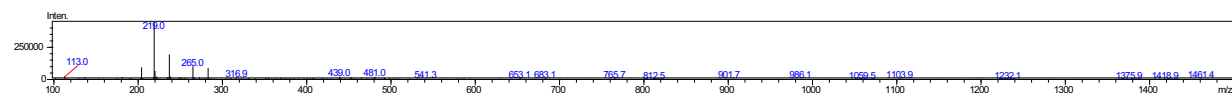
Fig. S2.14. A compilation of clusters with ψ ACP fusion proteins. The *tin* cluster is well conserved across *Trichoderma* strains, and only one example is shown here. Besides ψ ACP-MT, we also identified ψ ACP-TEs across different fungal strains in much less conserved clusters. The vestigial ACP motifs of each ψ ACP-TE are in parentheses.

2.15. SDS-PAGE analysis

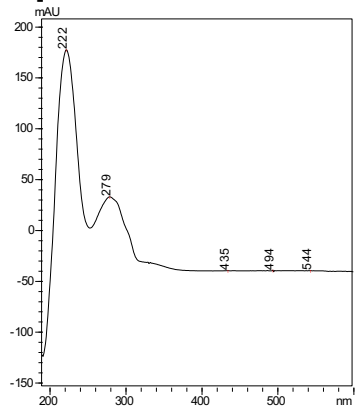




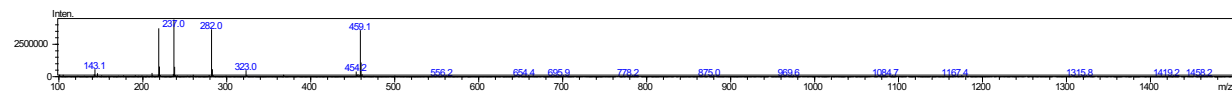
2.16. UV and MS spectra of compounds characterized in this study



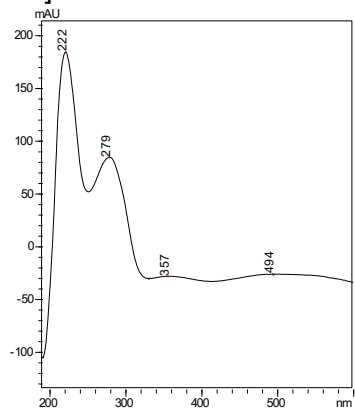
[M-H]⁻=219



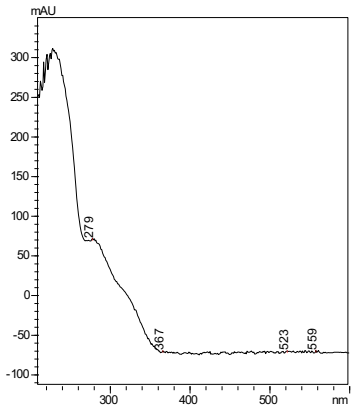
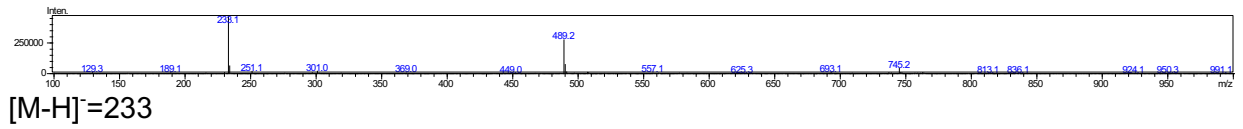
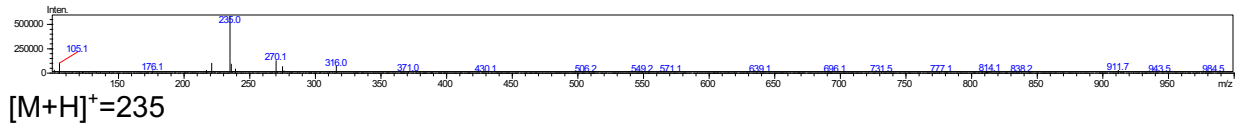
UV and MS spectra of 1.



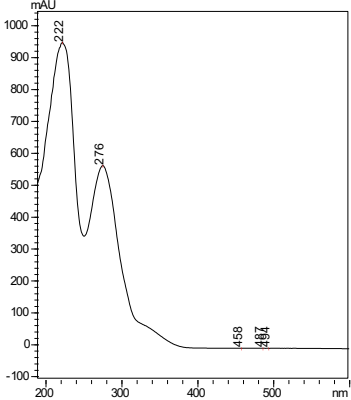
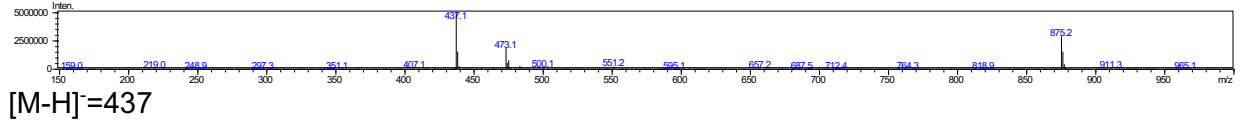
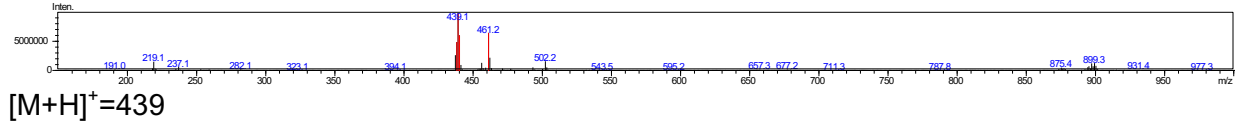
[M+H]⁺=219



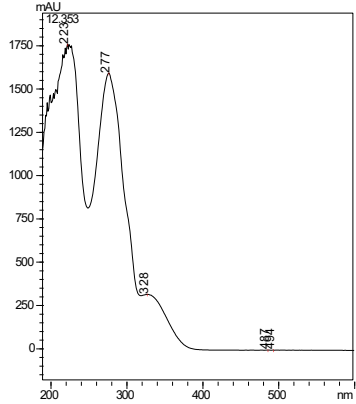
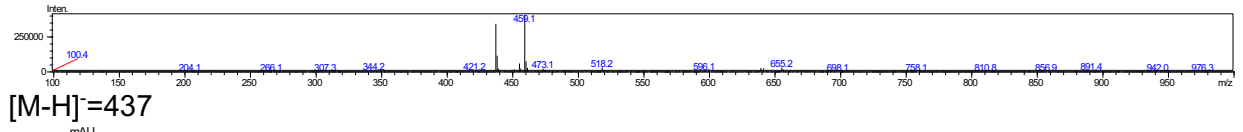
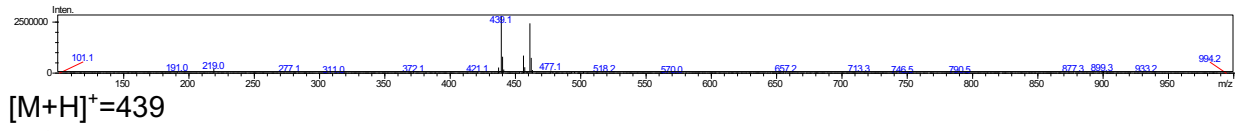
UV and MS spectra of 2.



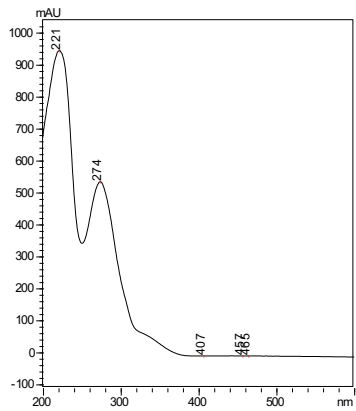
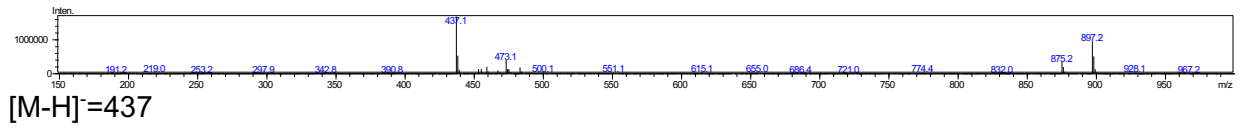
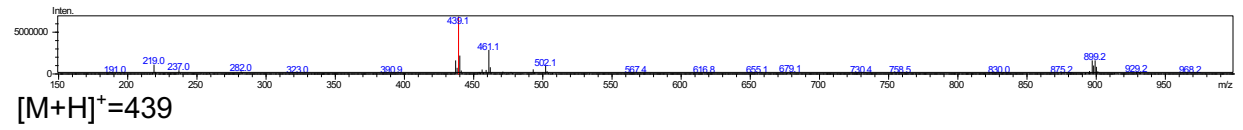
UV and MS spectra of **3**.



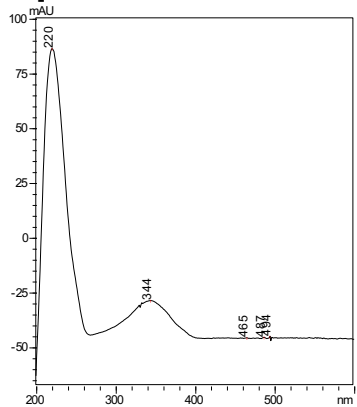
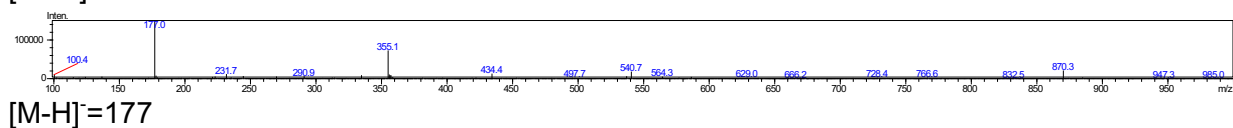
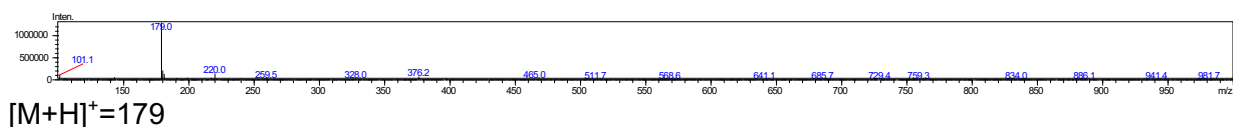
UV and MS spectra of **4**.



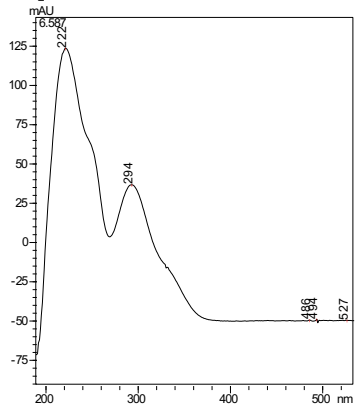
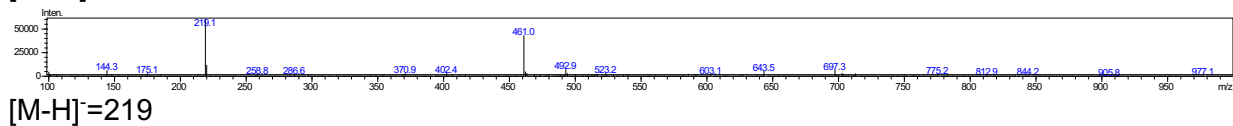
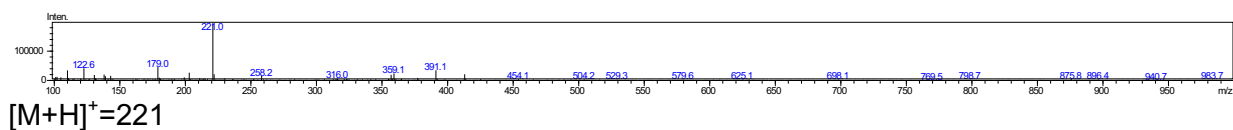
UV and MS spectra of **4**.



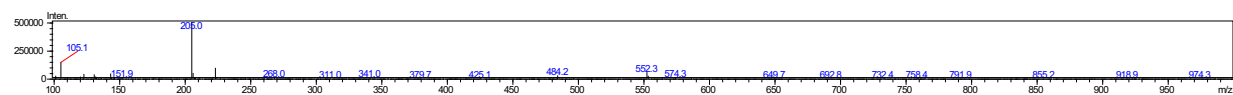
UV and MS spectra of **5**.



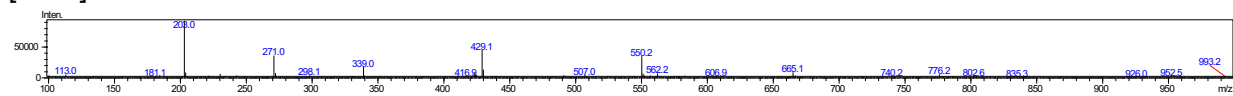
UV and MS spectra of **7**.



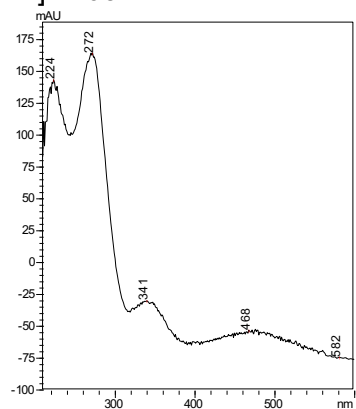
UV and MS spectra of **8**.



[M+H]⁺=205



[M-H]⁻=203



UV and MS spectra of **9(9')**.

3. Tables

Table S1. Primers used in this study.

Name	Sequence
pMC001F	CTATCAACTATTA ACTATATCGTAATCATATGGCTACAGCAGGGAATGAC GGCACATC
pMC001R	TGATAATGAAA ACTATAAATCGTGAAGGTTACTATTCTTGCTACAAAGC GCCGACGC
pMC002F	TCAACTATTA ACTATATCGTAATACCATATGACGGCAACCACAAAACGAC ATCTCC
pMC002R	AATGGAACTATAAATCGTGAAGGCATTTATCAGAGCATCTCGTG CAGT GCACGTTTC
pMC003F	CAGCAGCCATCATCATCATCACAGCAGCGGCTCACTCGAAAAAGTT CGTGAAATTTT
pMC003R	AAAAATCTTTGACTATTCAATCATTGCGCCTAACTCGCATAACCCAATAAT CAAGCGCTGC
pMC004F	CAACTATTA ACTATATCGTAATACCATATGCCAAATACCGCTGTCAGTCC CAAGGAG
pMC004R	GCATCGGTCCGCACAAATTTGTCTTATTACTTGATGATATTTTTAAGAGG C
pMC005F1	GTCAACTCTATCCTCAA AATACAATACAAATGCCAATTCGCGTCATTAT TGTCGGC
pMC005R1	AATCTTTGACTATTCAATCATTGCGCTTATACATCTGAAGCAAGACTTTT CTCCAA
pMC005F2	CAACTATTA ACTATATCGTAATACCATATGGCGCAATCAGACCTTACT CGAG
pMC005R2	TAATGAAA ACTATAAATCGTGAAGGCATCTATGCGTTGAAGAGAATATCG ATAATTC
pMC005F3	GCATAACATAACAAAAAGTCAACGAAAAATGCCAATACCGCTGTCAGT CCCAAGG
pMC005R3	AGTGGTAGATTGGGCTACGTAAATTCGATTACTTGATGATATTTTTAAGA GGCTGC
overlap_T34A _fw	GGATGAGCTTGGAGTCGACGCAATCTTGGCCAAGAAGACTG
overlap_T34A _rv	CAGTTCTTTGGCCAAGATTGCGTCGACTCCAAGCTCATCC
overlap_T34s _fw	GGATGAGCTTGGAGTCGACTCAATCTTGGCCAAGAAGACTG

overlap_T34s	
_rv	CAGTTCTTTGGCCAAGATTGAGTCGACTCCAAGCTCATCC
pMC006F	GCTAGCGATTATAAGGATGATGATGATAAGGCTACAGCAGGGAATGAC GGCACATCTATT
pMC006R	TCATTTAAATTAGTGATGGTGATGGTGATGTTCTTGCTACAAAGCGCC GACGCATTTGC
pMC007F	CAACTATTAATATATCGTAATACCATATGACGGCAACCACAAAACGACA TCTCC
pMC007R	TTTAAATTAGTGATGGTGATGGTGATGATGGTGGAGCATCTCGTGCACT GCACGTTTCAC
pMC008F	TATCAACTATTAATATATCGTAATACCATATGCCAAATACCGCTGTCAG TCCCAAGGAG
pMC008R	ATTTAAATTAGTGATGGTGATGGTGATGGTGATGTGACCTGTTCCGCCA TCTTTGCCAAT
pMC009F	TATCAACTATTAATATATCGTAATACCATATGCCAATTCGCGTCATTATT GTCGGCGCT
pMC009R	TTTAAATTAGTGATGGTGATGGTGATGGTGATGTACATCTGAAGCAAGA CTTTTCTCCAA
pMC010F	TACTTCCAATCCAATGCAATGTCACTCGAAAAAGTTTCGTG
pMC010R	TTATCCACTTCCAATGTTATTACTAACTCGCATAACCAATAATCAAGC
pMC011F	TACTTCCAATCCAATGCAGAGACACCATCCAGAAAACAGTCGC
pMC015F	TACTTCCAATCCAATGCAATGACGGCAACCACAAAACGACATCTCCTA
pMC015R	TTATCCACTTCCAATGTTATTATTTTTTCGACAACCGGAGAAGGAGCTGT
MAT0_S991_f	
w	TGATGCTGTCCTTGGTCACGCCCTTG
MAT0_S991_	
rv	CAAGGGCGTGACCAAGGACAGCATCA
pMC016F	TACTTCCAATCCAATGCAGAGCCCCAAGCCTCCGACGACTCTGCTTC TTATCCACTTCCAATGTTATTATCAGAGCATCTCGTGACGTGCACGTTTC
pMC016R	AC
pMC017R	TTATCCACTTCCAATGTTATTAGTTGACCGTGGGCTCCATATGCGACTGT
pMC011F	TACTTCCAATCCAATGCAGAGACACCATCCAGAAAACAGTCGC GAAAACCTGTACTTCCAATCCAATATTACCGAAGAGGTGCGCAACCTTG
pMC019F	T
pMC019R	AATTCGGATCCGTTATCCACTTCCAATTTATTCAGCTTCACTGGCTTCGT CCTC

pMC020F	GTTTAACTTTAAGAAGGAGATATAGTTATGCCAATTCGCGTCATTATTGT CGGC
pMC020R	GATGAGAGCCGGATTGGAAGTAGAGGTTTACATCTGAAGCAAGACTTTT CTCCAAA
pMC021F	TACTTCCAATCCAATGCAATGGCGCAATCAGACCTTACACTCGAGAGC TTATCCACTTCCAATGTTATTACTATGCGTTGAAGAGAATATCGATAATT
pMC021R	CC

Table S2. Deduced functions of *tln* cluster genes.

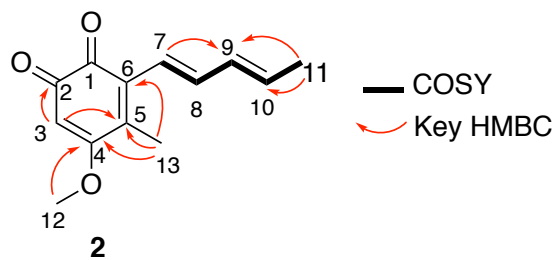
Gene name	Deduced function	Protein homolog	Accession	Identity %
TlnA	HRPKS (KS-AT-DH-ER ⁰ -KR-ACP)	ZEA2	A0A098D8A0	37
TlnB	NRPKS (SAT-KS-MAT-PT-ACP)	PKS16	E9KMQ2	38
TlnC	ψACP-MT	CitS	A0A161CEU9	52
TlnD	Thioesterase	TerA	Q0D1N9	31
TlnE	Flavin-dependent monooxygenase	3HBH1	Q9F131	32
TlnF	O-methyltransferase	Grayanic acid O-methyltransferase	E9KMQ4	33
TlnI	Transcription factor	SirZ	Q6Q877	45
TlnJ	Transporter	FUM19	Q8J2Q1	39

GenBank assembly accession code of *T. harzianum* genome sequence is GCA_000988865.1.

Table S3. Plasmids used for protein expression in this study.

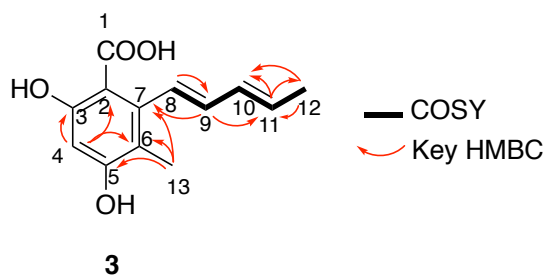
Protein	Plasmid name	Parent vector	Tag	Reference
TlnA	pMC006	xw55	N-FLAG, C-His6	This study
TlnB	pMC007	xw55	C-His8	This study
TlnD	pMC008	xw55	C-His8	This study
TlnE	pMC009	xw55	C-His8	This study
TlnC	pMC010	LIC-NTH	N-His6	This study
Δ TlnC	pMC011	LIC-NTH	N-His6	This study
T34A-TlnC	pMC012	LIC-NTH	N-His6	This study
T34S-TlnC	pMC013	LIC-NTH	N-His6	This study
SAT-KS-MAT	pMC014	LIC-NTH	N-His6	This study
SAT-KS-MAT ⁰	pMC015	LIC-NTH	N-His6	This study
TlnB-ACP	pMC016	LIC-NTH	N-His6	This study
ψ ACP	pMC017	LIC-NTH	N-His6	This study
T34S ψ ACP	pMC018	LIC-NTH	N-His6	This study
ACP _{CM}	pMC019	LIC-NTH	N-His6	This study
ACP _{P4}	pWZ248	pET28a	N-His6	4
TlnE	pMC020	LIC-NTH	C-His6	This study
TlnF	pMC021	LIC-NTH	N-His6	This study
NpgA	pSMa24	pET28a	N-His6	1

Table S4. ^1H (500 MHz) and ^{13}C (125 MHz) NMR data of **2** in CD_3OD .



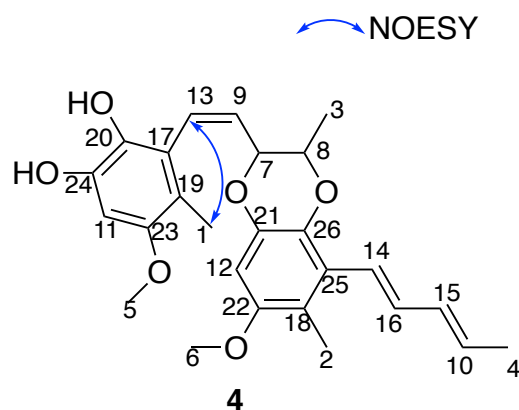
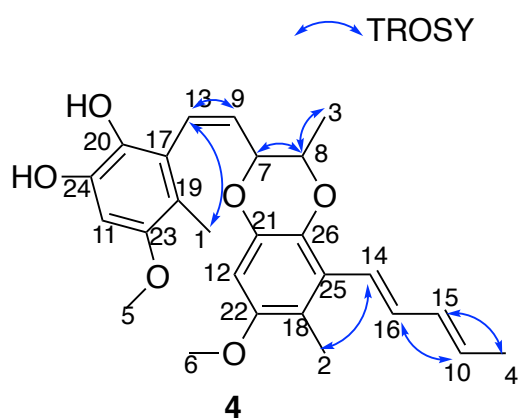
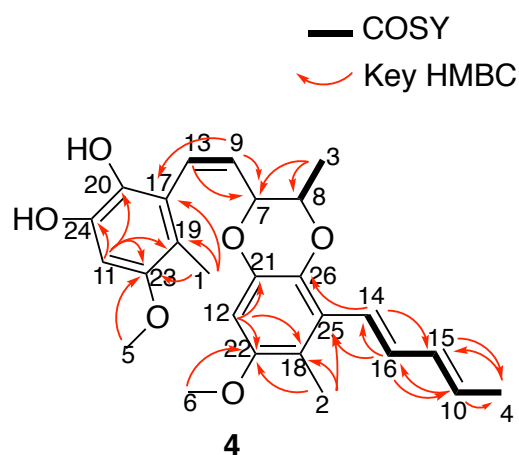
Pos.	δ_{C}	δ_{H} , multi, (<i>J</i> in Hz)
1	181.0, C	-
2	182.6, C	-
3	102.4, CH	5.83, s
4	174.0, C	-
5	143.6, C	-
6	137.0, C	-
7	123.0, CH	6.37, d, 15.7
8	141.6, CH	7.13, dd, 15.7, 10.7
9	135.1, CH	6.26, dd, 14.5, 10.2
10	135.7, CH	5.99, m, overlap
11	19.4, CH_3	1.86, d, 6.9
12	58.7, CH_3	3.96, s
13	14.7, CH_3	2.21, s

Table S5. ^1H (500 MHz) and ^{13}C (125 MHz) NMR data of **3** in CD_3OD .



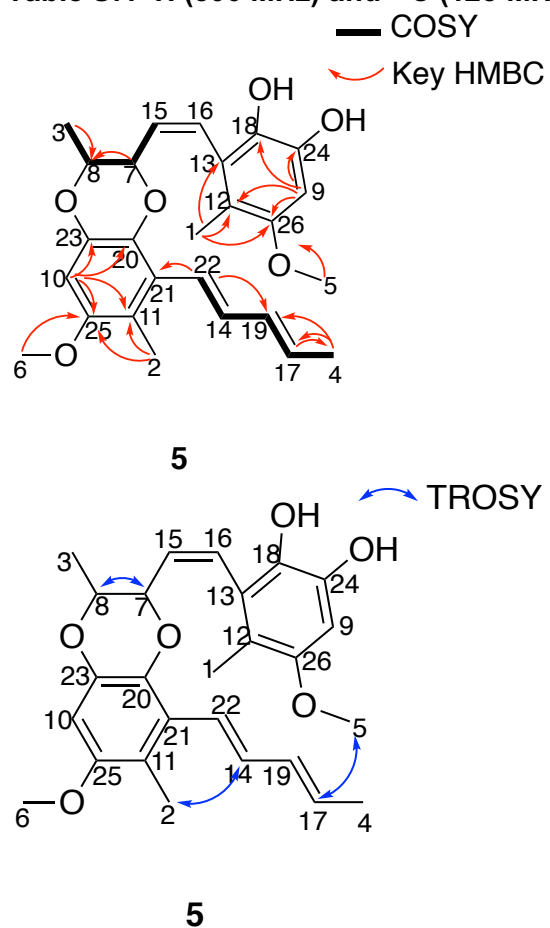
Pos.	δ_{C}	δ_{H} , multi, (J in Hz)
1	168.2, C	-
2	106.9, C	-
3	160.9, C	-
4	103.0, C	6.21, s
5	162.8, C	-
6	117.1, C	-
7	143.6, C	-
8	131.3, CH	6.87, d, 15.9
9	134.3, CH	5.98, dd, 15.9, 10.4
10	133.7, CH	6.21, m
11	129.0, CH	5.67, dq, 13.6, 6.8
12	18.3, CH_3	1.78, d, 6.7
13	13.4, CH_3	2.09, s

Table S6. ^1H (500 MHz) and ^{13}C (125 MHz) NMR data of **4** in CD_3OD .



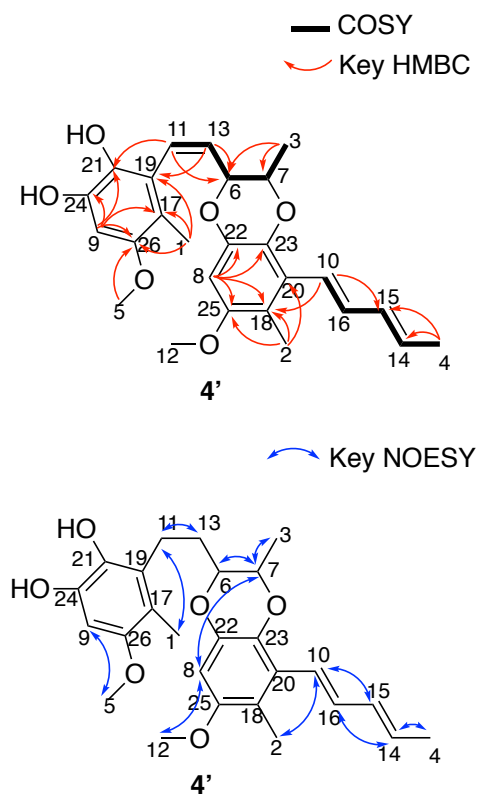
Pos.	δ_{C}	δ_{H} , multi, (J in Hz)
1	10.1, CH_3	2.04, s
2	12.3, CH_3	2.06, s
3	14.5, CH_3	1.25, d, 6.5
4	18.3, CH_3	1.80, d, 6.7
5	56.4, CH_3	3.72, s
6	56.2, CH_3	3.74, s
7	76.9, CH	4.87, masked by water peak
8	81.6, CH	4.12, dq, 6.5, 3.0
9	124.2, CH	5.65, dd, 10.2, 3.1
10	130.9, CH	5.78, m, overlap
11	101.4, CH	6.39, s
12	99.3, CH	6.40, s
13	123.9, CH	6.66, dd, 10.2, 2.2
14	125.6, CH	6.47, m, overlap
15	133.6, CH	6.24, qd, overlap
16	136.9, CH	6.61, q, 15.9, 10.4
17	122.5, C	-
18	116.9, C	-
19	113.9, C	-
20	143.8, C	-
21	149.7, C	-
22	155.7, C	-
23	153.2, C	-
24	135.9, C	-
25	133.1, C	-
26	136.9, C	-

Table S7. ^1H (500 MHz) and ^{13}C (125 MHz) NMR data of **5** in CD_3OD .



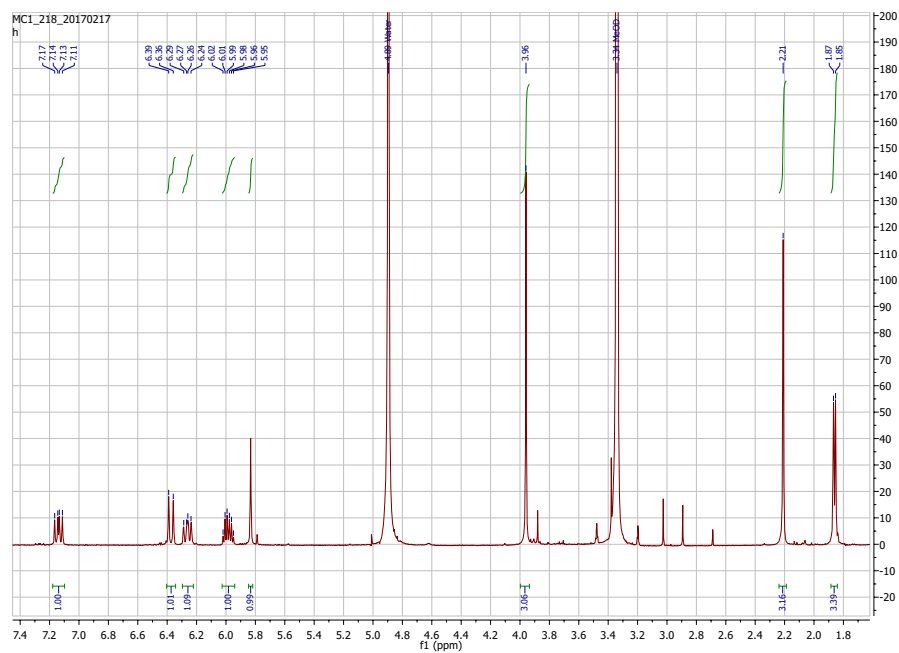
Pos.	δ_{C}	δ_{H} , multi, (J in Hz)
1	11.0, CH_3	2.10, s
2	13.5, CH_3	2.10, s
3	15.9, CH_3	1.15, d, 6.4
4	19.1, CH_3	1.78, m
5	57.1, CH_3	3.77, s
6	57.2, CH_3	3.77, s
7	78.7, CH	4.90, masked by water peak
8	79.8, CH	4.47, m
9	100.4, CH	6.43, m, overlap
10	102.2, CH	6.44, m, overlap
11	114.8, C	-
12	117.4, C	-
13	123.6, C	-
14	124.6, C	6.76, m
15	124.9, C	5.97, m, overlap
16	126.8, C	6.40, s
17	131.6, C	5.73, m, overlap
18	134.4, C	-
19	134.4, C	5.98, m, overlap
20	136.2, C	-
21	137.5, C	-
22	138.1, C	6.44, m, overlap
23	144.9, C	-
24	150.4, C	-
25	154.2, C	-
26	156.6, C	-

Table S8. ^1H (500 MHz) and ^{13}C (125 MHz) NMR data of **4'** in CD_3OD .

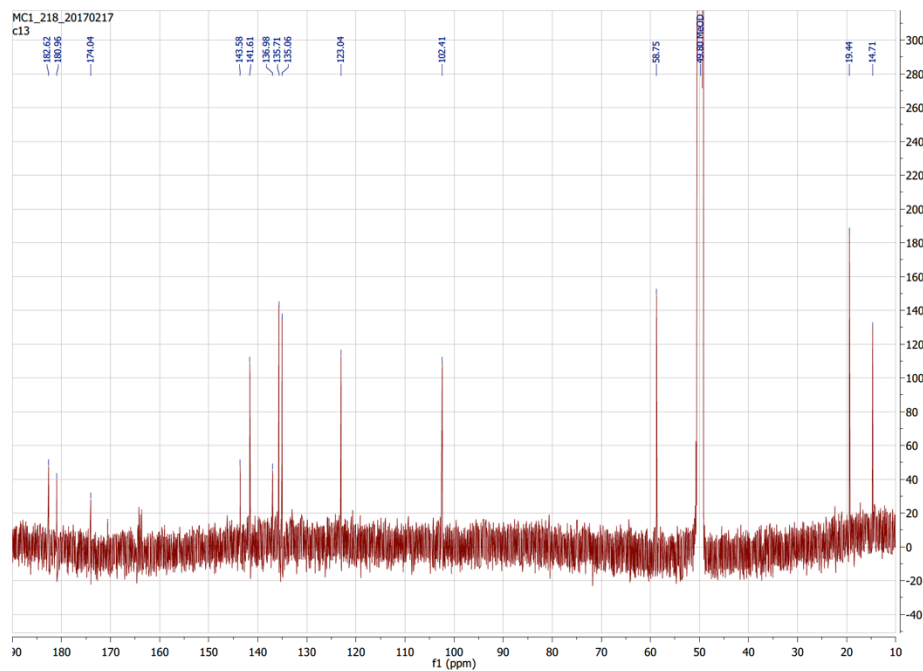


Pos.	δ_{C}	δ_{H} , multi, (J in Hz)
1	11.0, CH ₃	2.09, s
2	13.3, CH ₃	2.15, s
3	16.0, CH ₃	1.42, d, 6.3
4	19.3, CH ₃	1.83, d, 6.8
5	57.3, CH ₃	3.75, s
6	78.2, CH	4.96, td, 3.5, 2.0
7	80.7, CH	4.55, m
8	102.2, CH	6.61, s
9	102.4, CH	6.42, s
10	126.5, CH	6.50, m
11	125.1, CH	6.80, m, overlap
12	57.9, CH ₃	3.75, s
13	125.0, CH	5.92, dd, 10.2, 3.4
14	130.8, CH	5.78, m
15	135.4, CH	6.26, m
16	137.2, CH	6.87, m
17	114.9, C	-
18	120.4, C	-
19	123.3, C	-
20	127.2, C	-
21	136.8, C	-
22	144.7, C	-
23	142.3, C	-
24	144.6, C	-
25	152.8, C	-
26	154.2, C	-

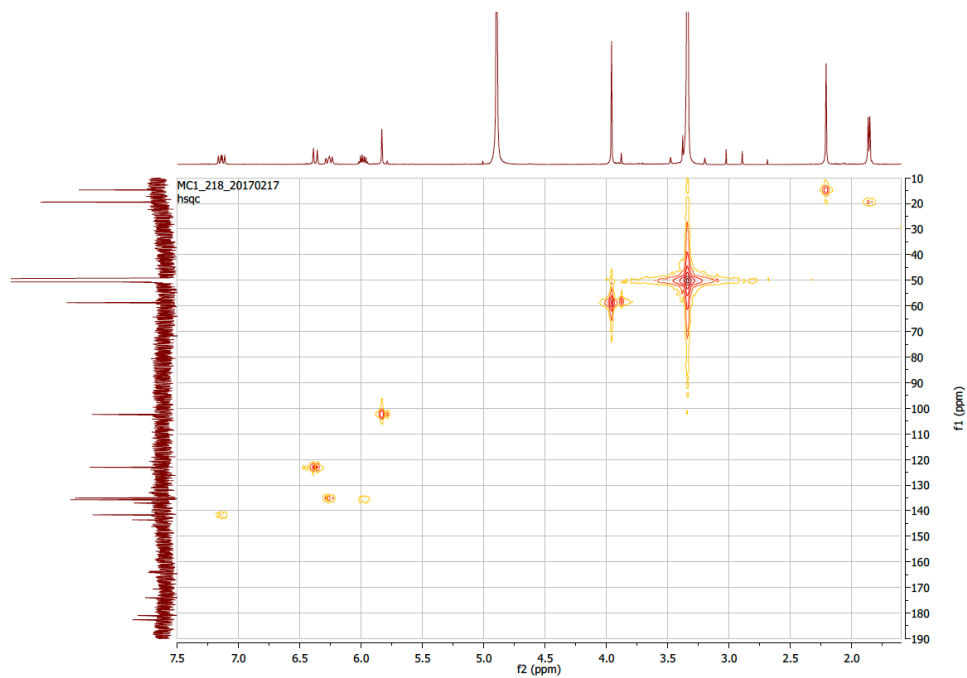
NMR spectra of compounds characterized in this study



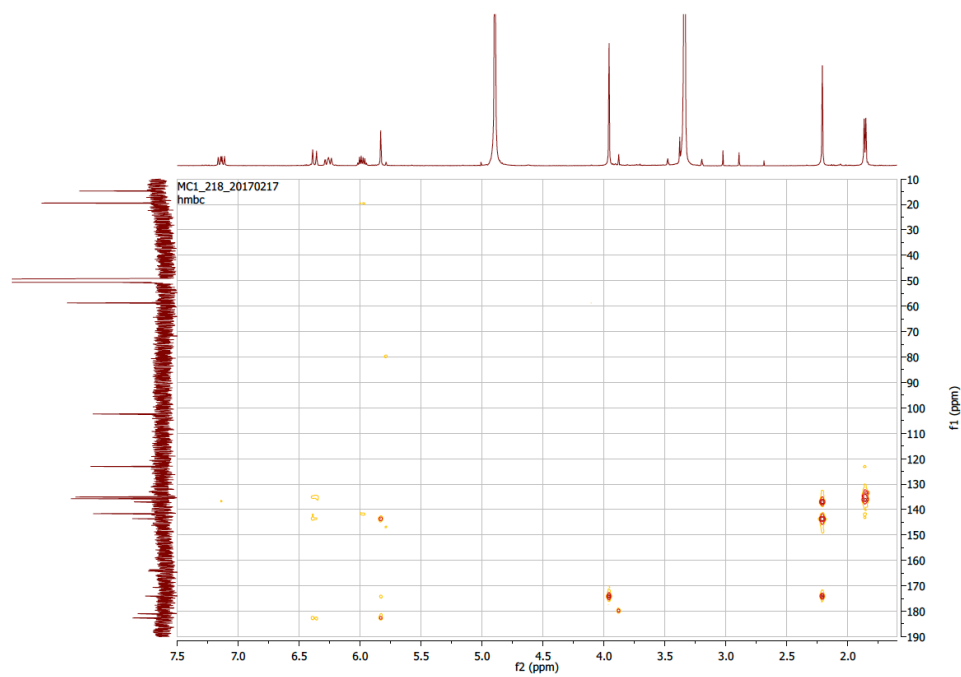
^1H NMR spectrum of **2** in CD_3OD (500 MHz).



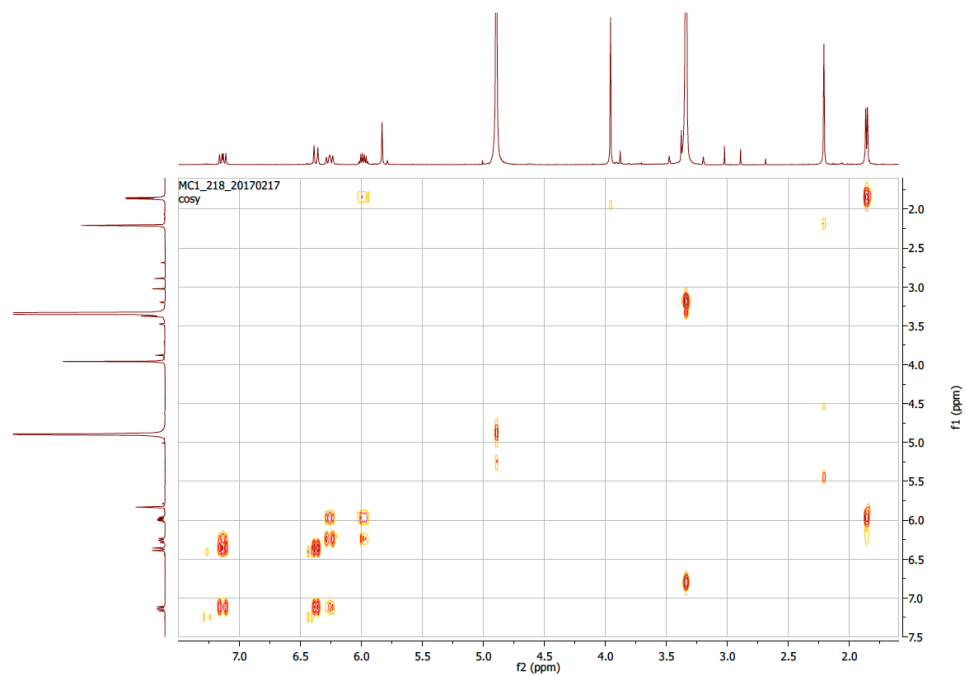
^{13}C NMR spectrum of **2** in CD_3OD (125 MHz).



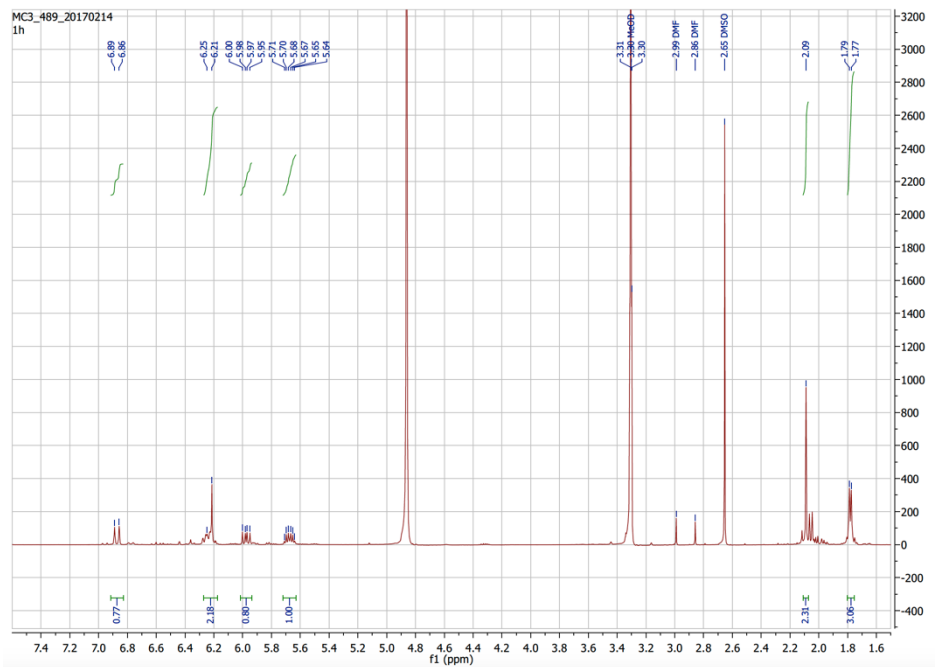
HSQC spectrum of **2** in CD₃OD (500 MHz).



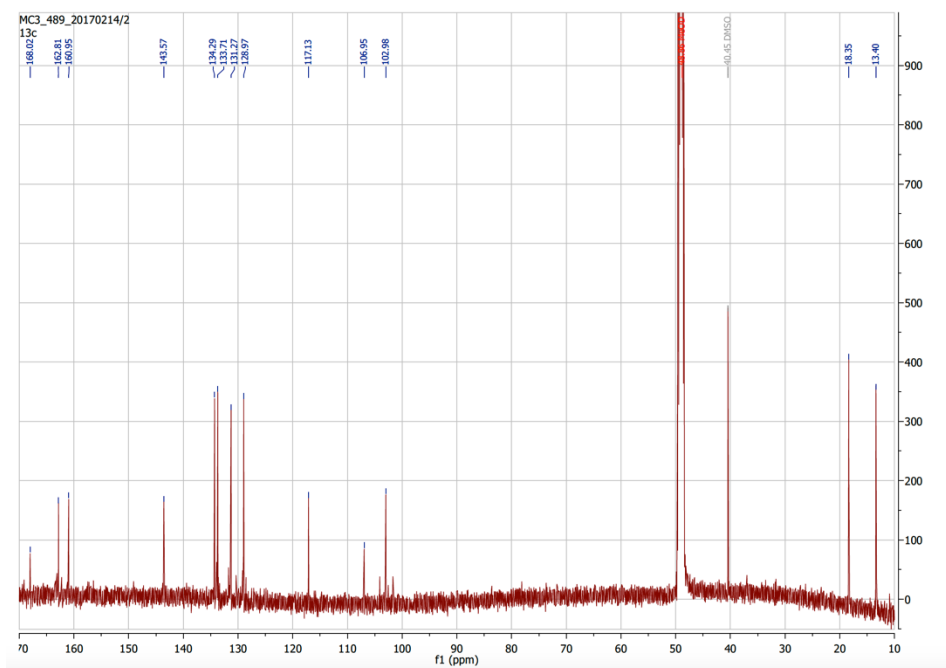
HMBC spectrum of **2** in CD₃OD (500 MHz).



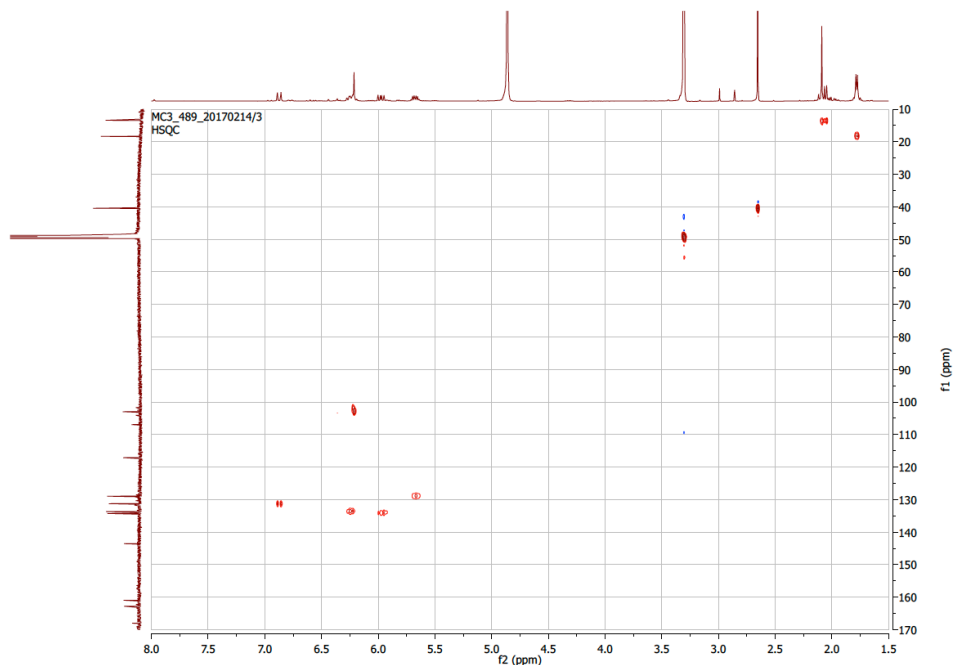
COSY spectrum of **2** in CD₃OD (500 MHz).



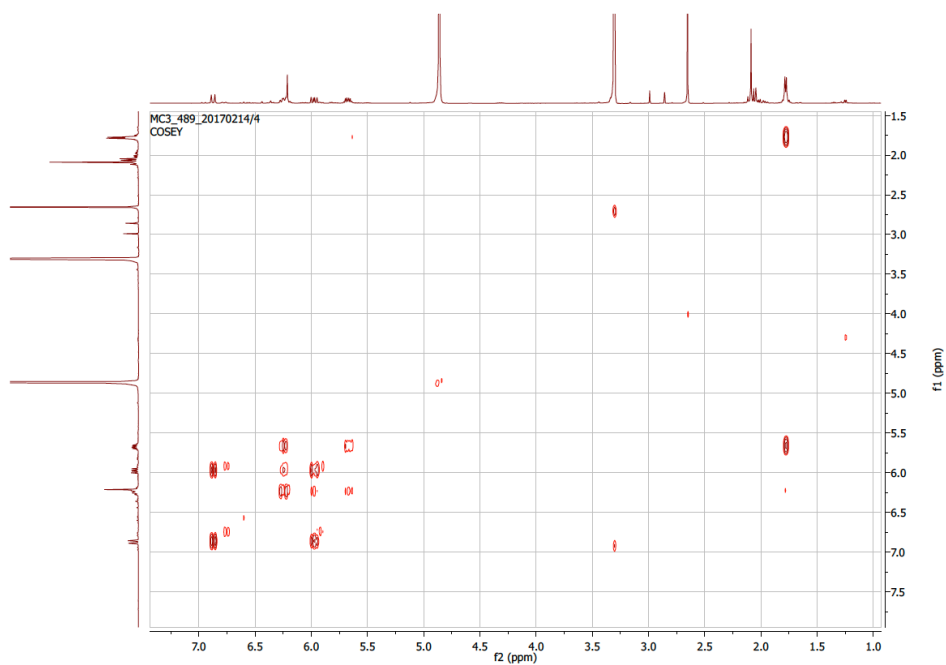
^1H NMR spectrum of **3** in CD_3OD (500 MHz).



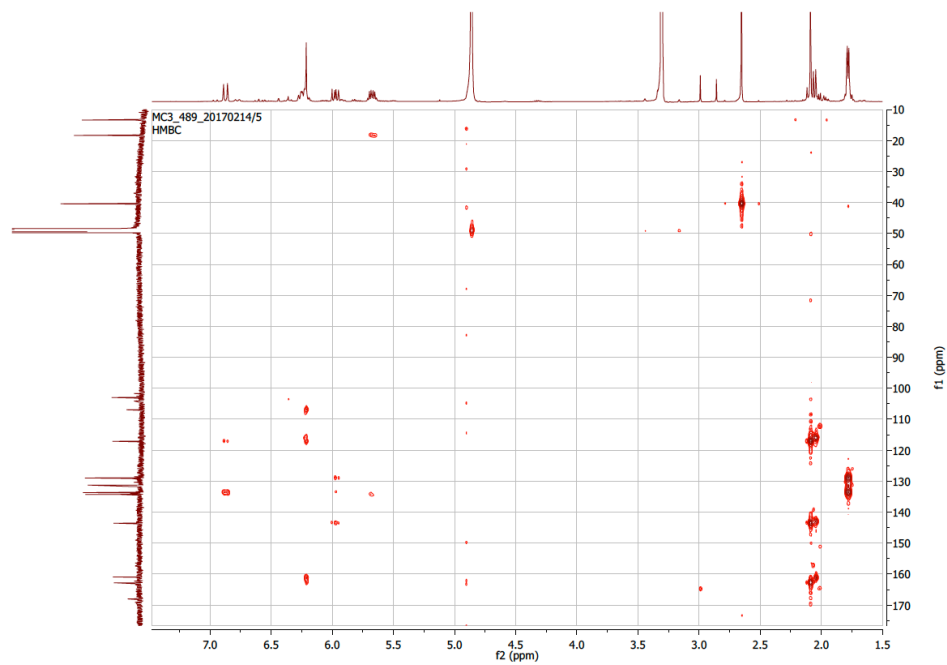
^{13}C NMR spectrum of **3** in CD_3OD (125 MHz).



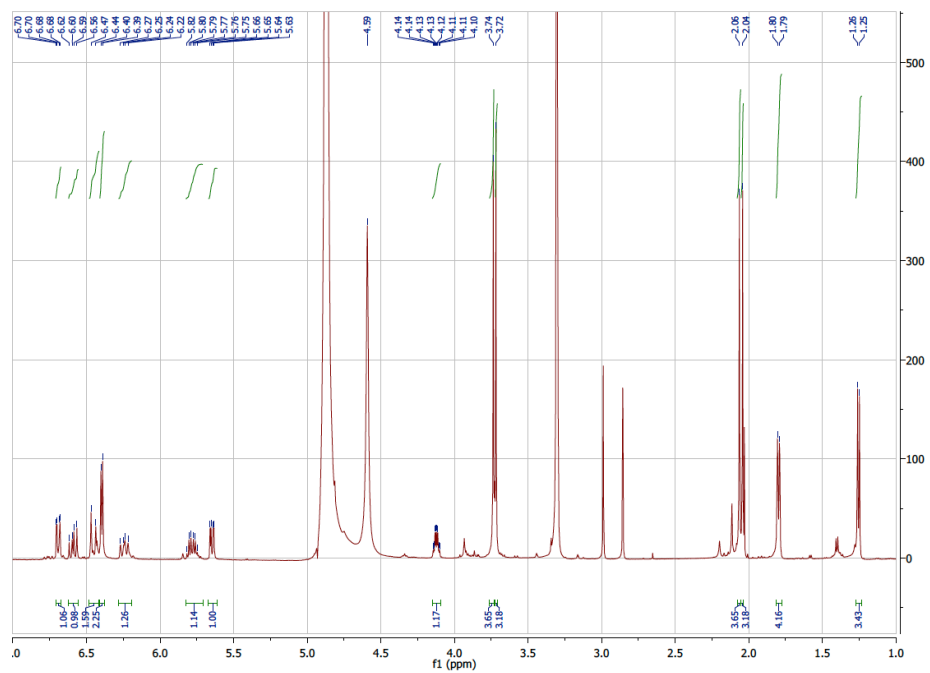
HSQC spectrum of **3** in CD₃OD (500 MHz).



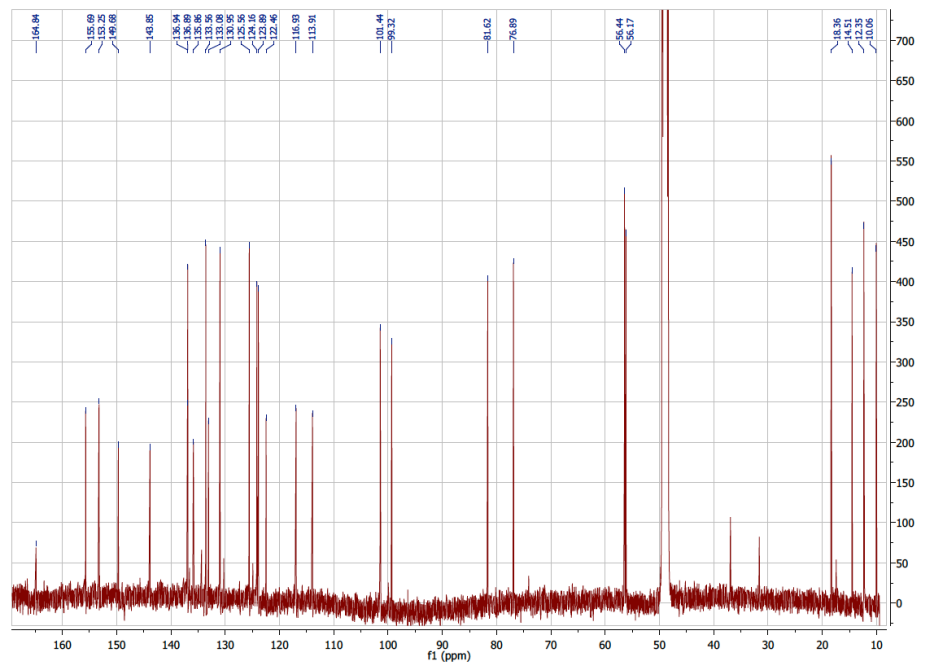
COSY spectrum of **3** in CD₃OD (500 MHz).



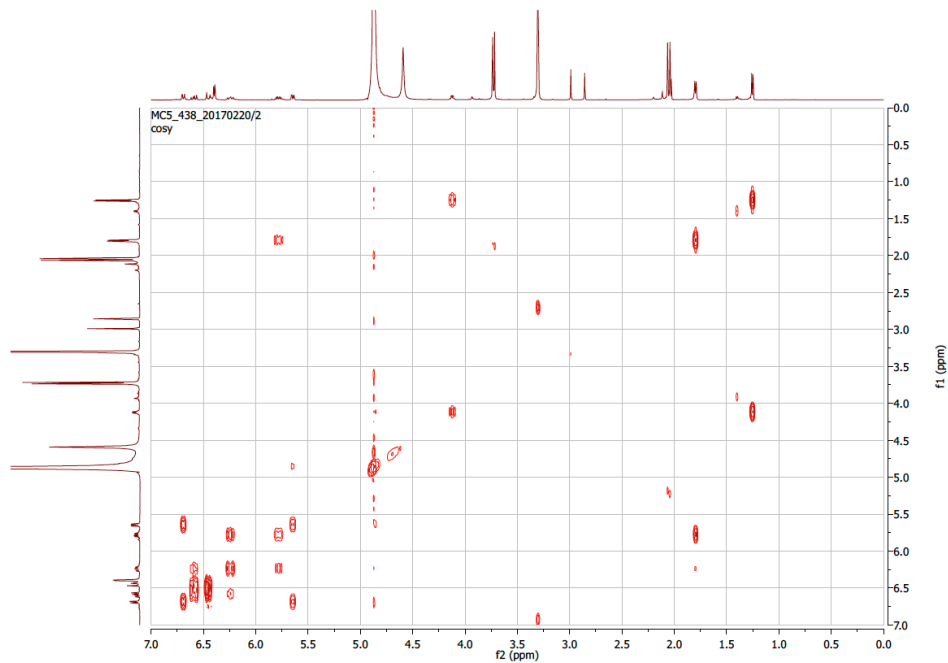
HMBC spectrum of **3** in CD₃OD (500 MHz).



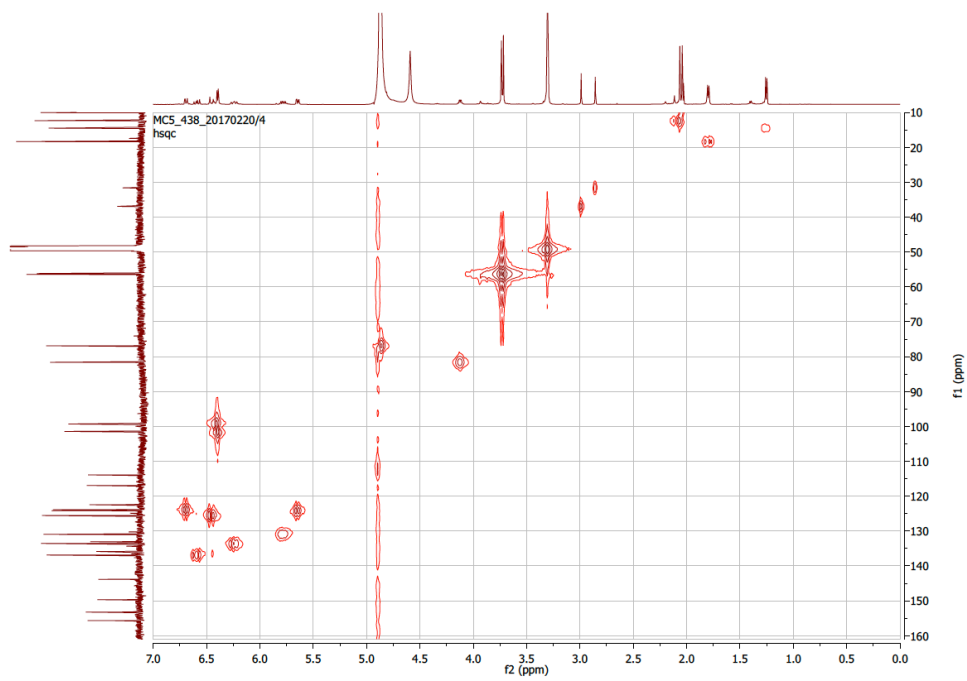
^1H NMR spectrum of **4** in CD_3OD (500 MHz).



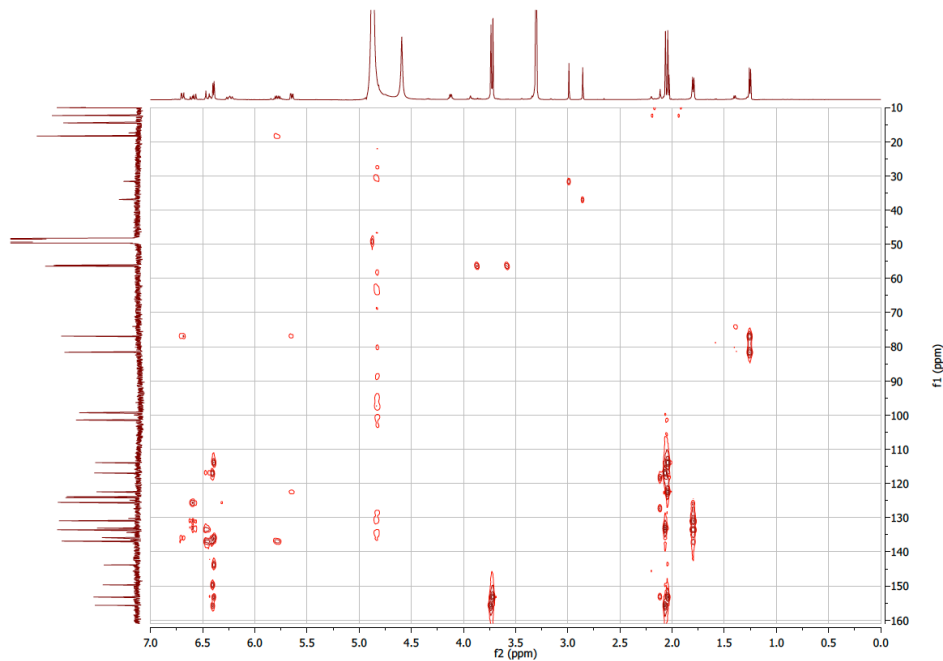
^{13}C NMR spectrum of **4** in CD_3OD (125 MHz).



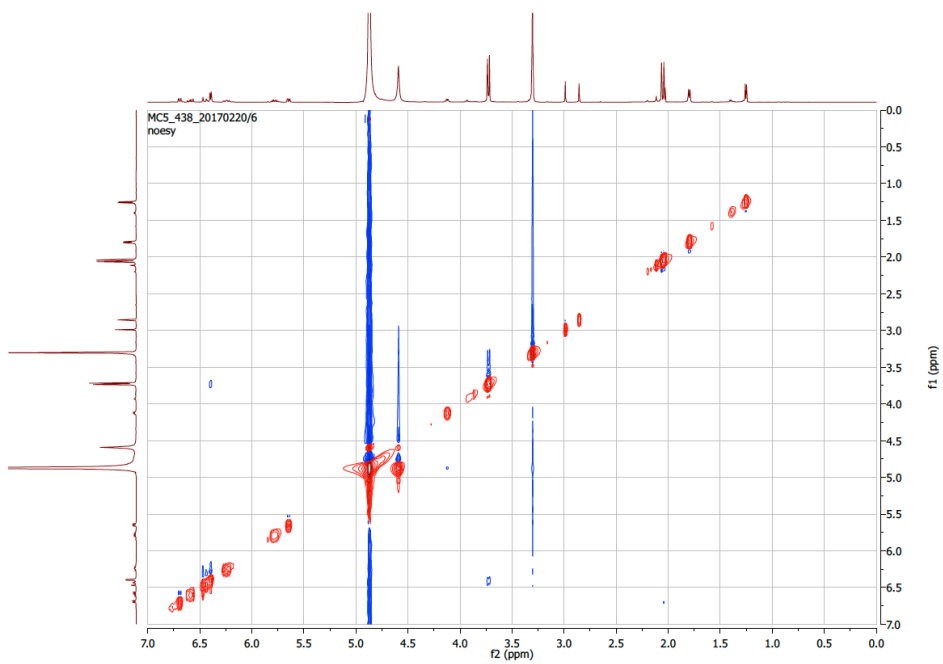
COSY spectrum of **4** in CD₃OD (500 MHz).



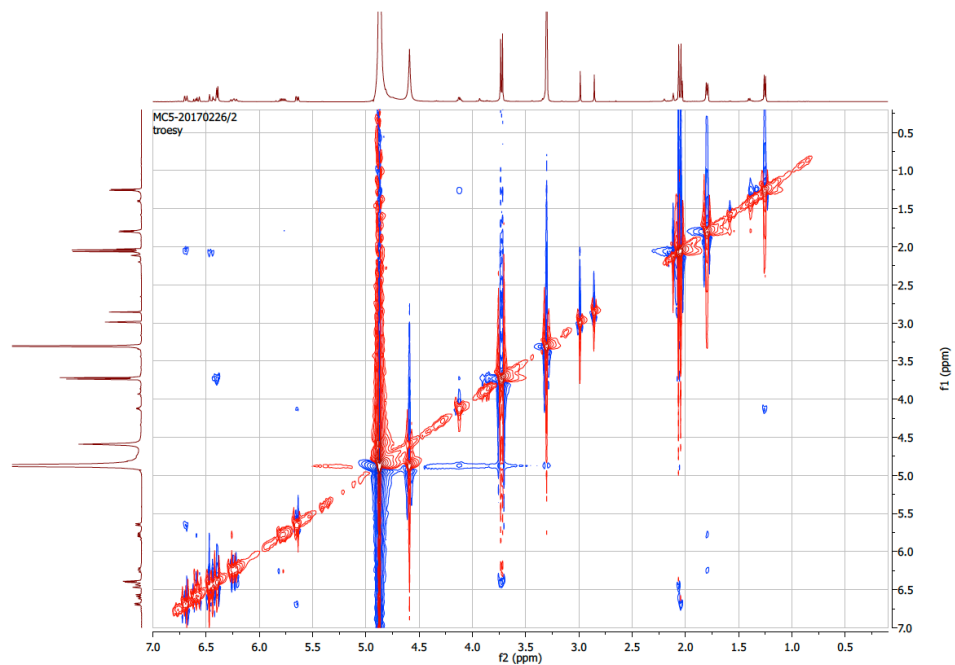
HSQC spectrum of **4** in CD₃OD (500 MHz).



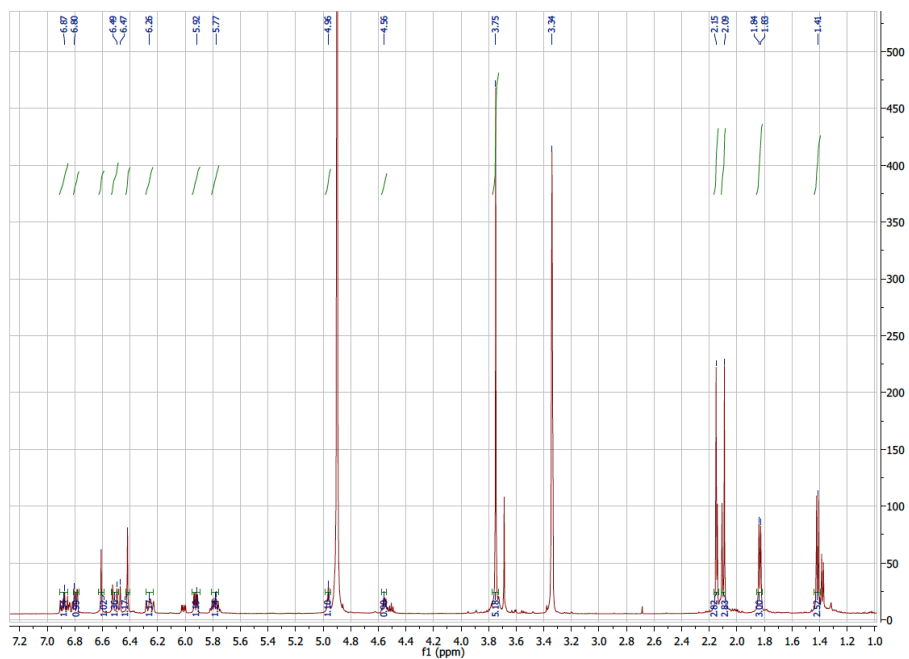
HMBC spectrum of **4** in CD₃OD (500 MHz).



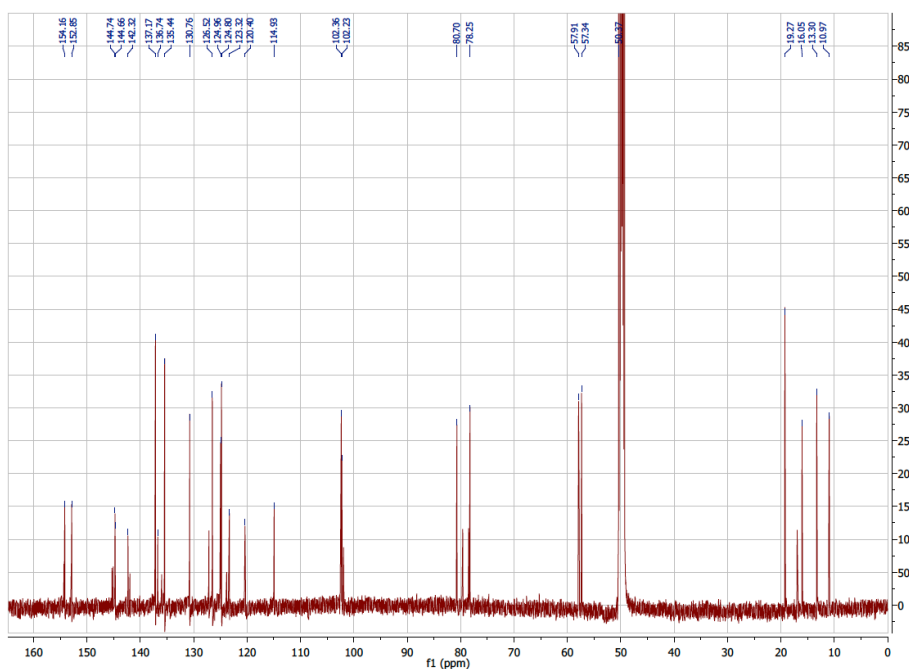
NOESY spectrum of **4** in CD₃OD (500 MHz).



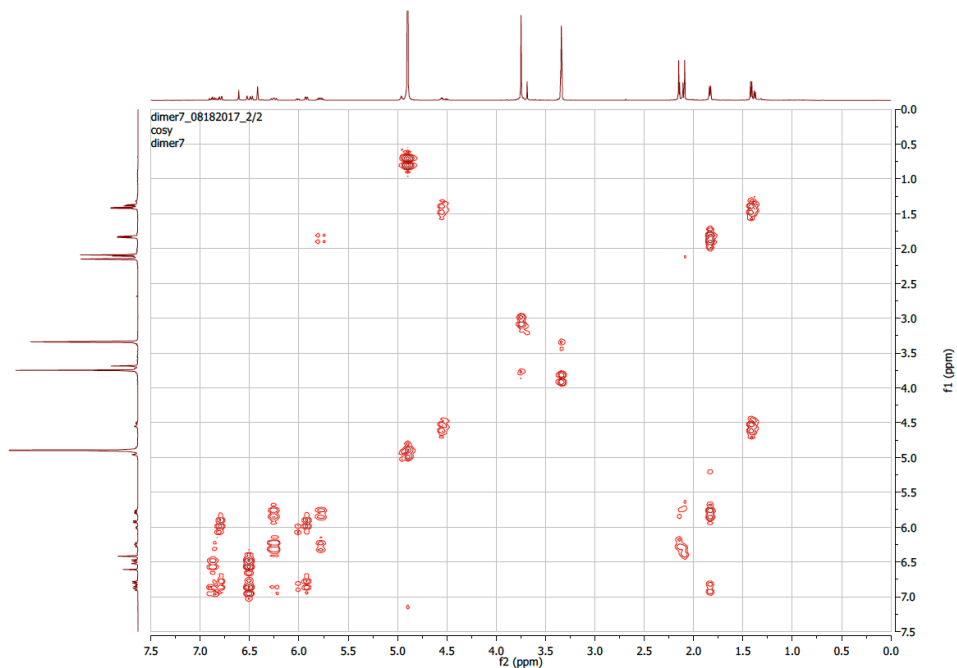
TROSY spectrum of **4** in CD₃OD (500 MHz).



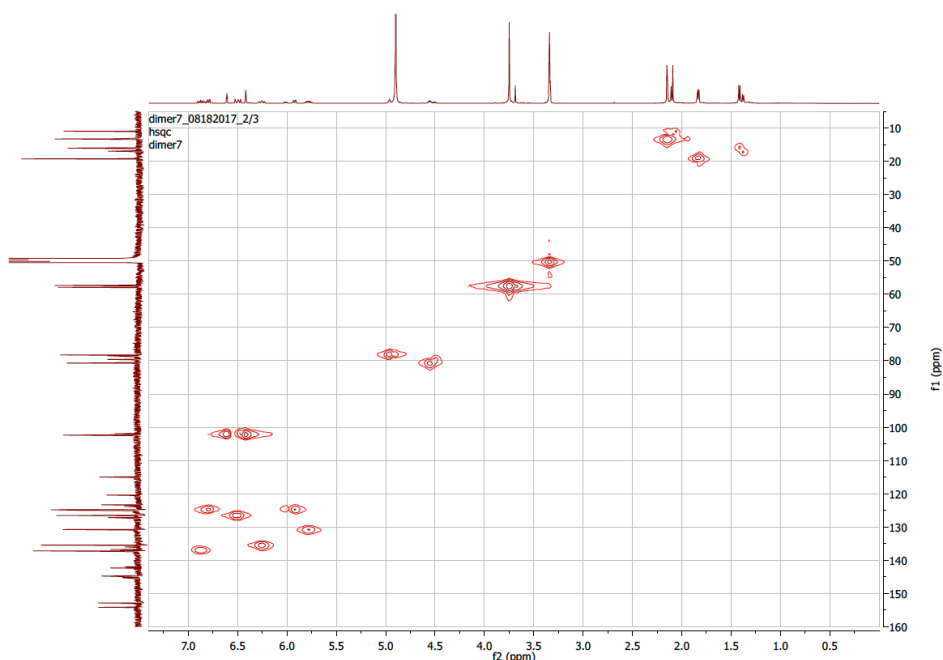
¹H spectrum of 4' in CD₃OD (500 MHz).



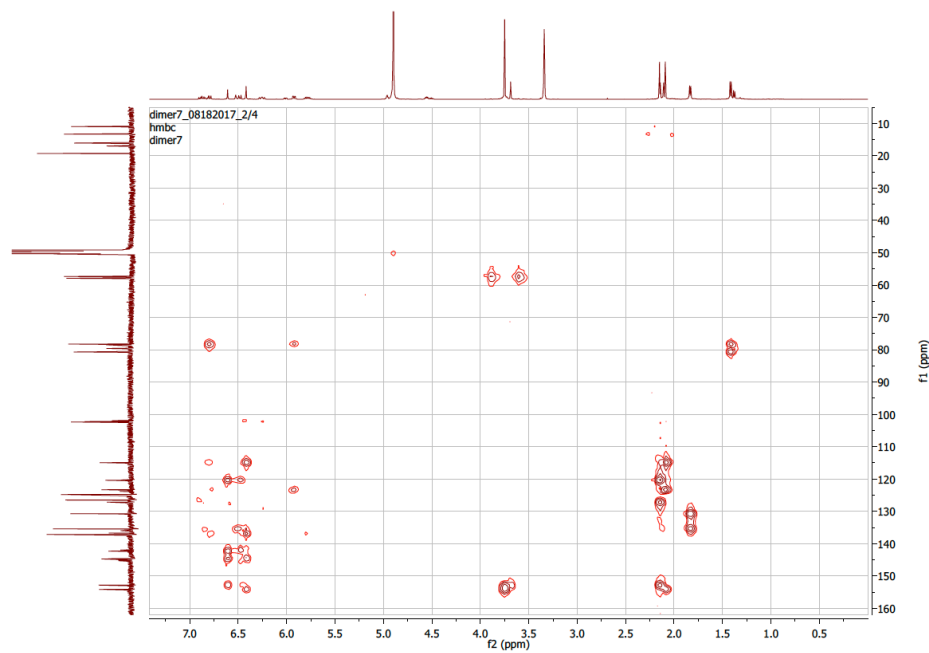
¹³C spectrum of 4' in CD₃OD (125 MHz).



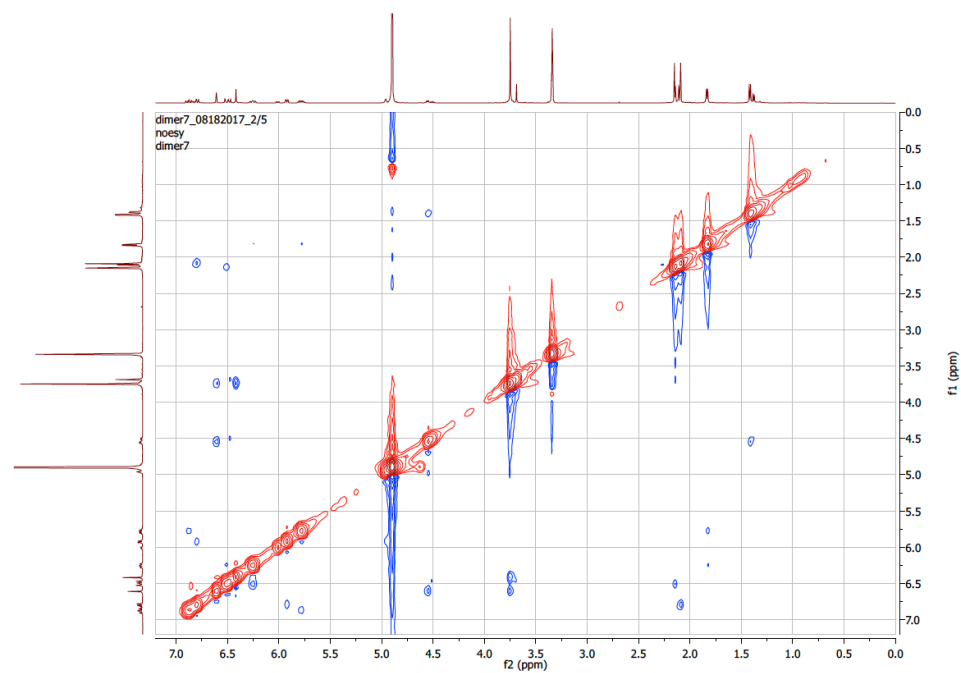
COSY spectrum of **4'** in CD₃OD (500 MHz).



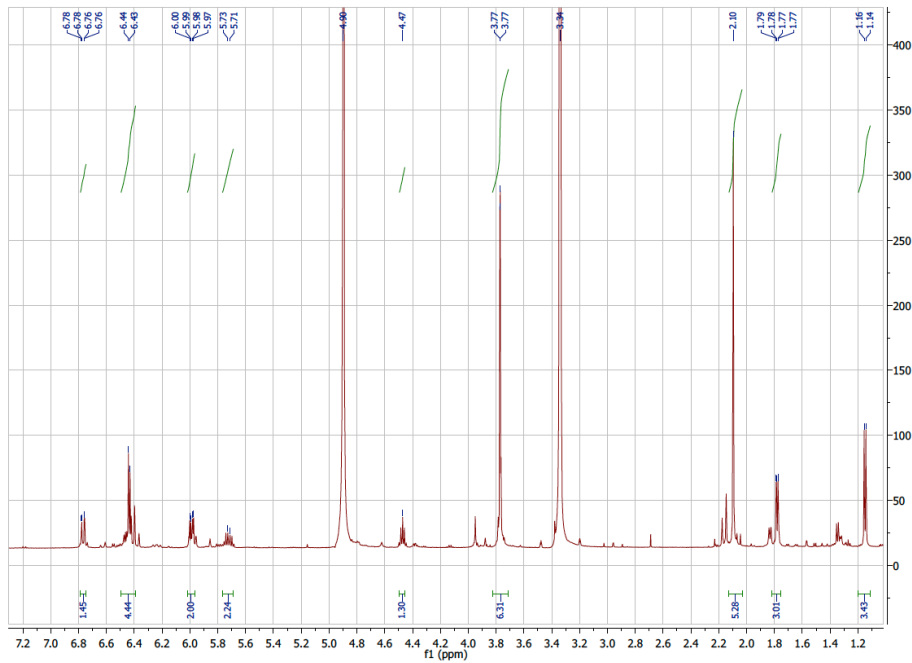
HSQC spectrum of **4'** in CD₃OD (500 MHz).



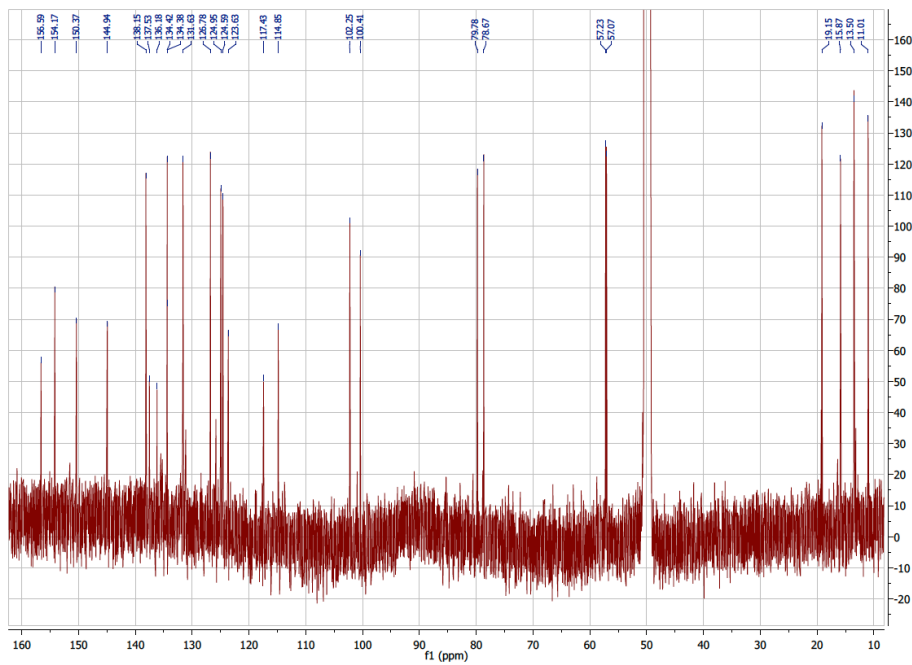
HMBC spectrum of **4'** in CD₃OD (500 MHz).



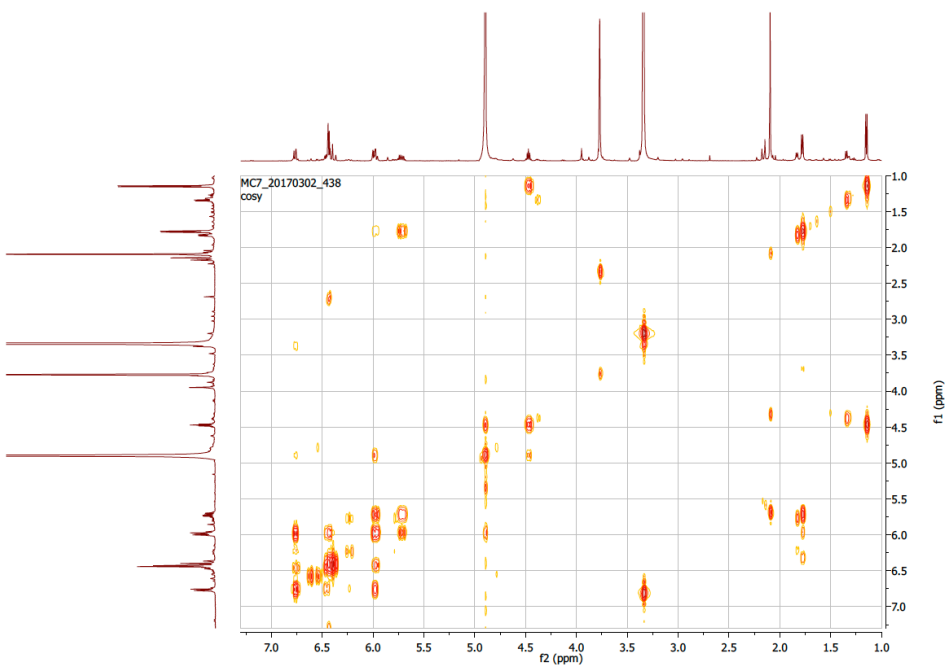
NOESY spectrum of **4'** in CD₃OD (500 MHz).



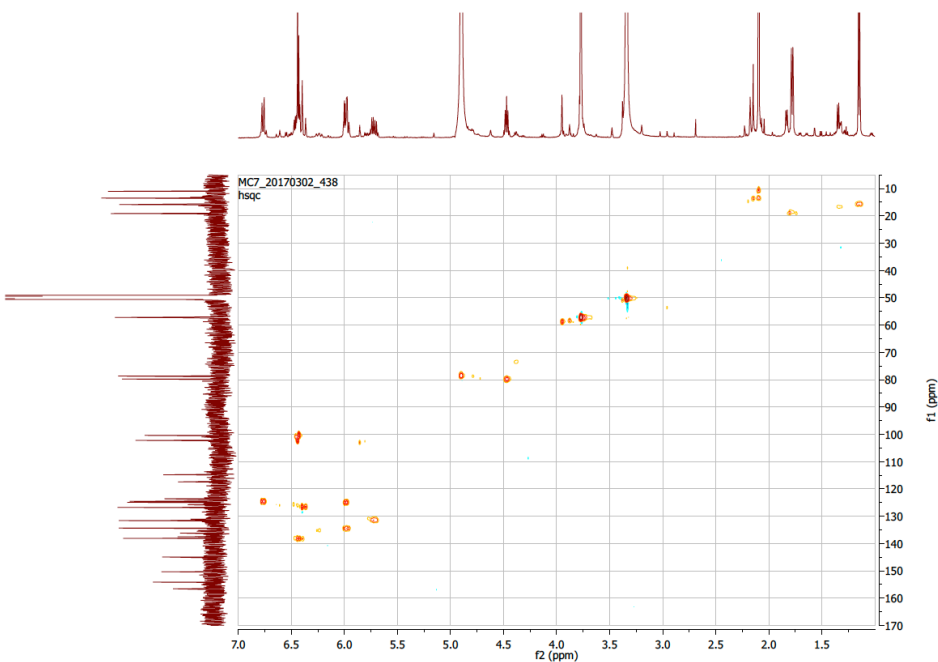
¹H spectrum of **5** in CD₃OD (500 MHz).



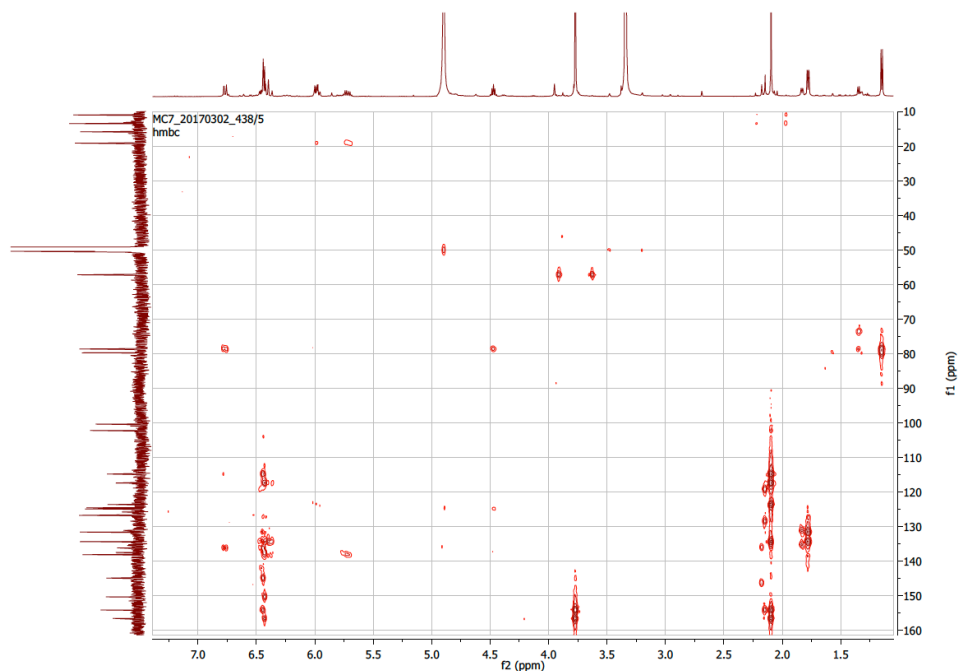
¹³C spectrum of **5** in CD₃OD (125 MHz).



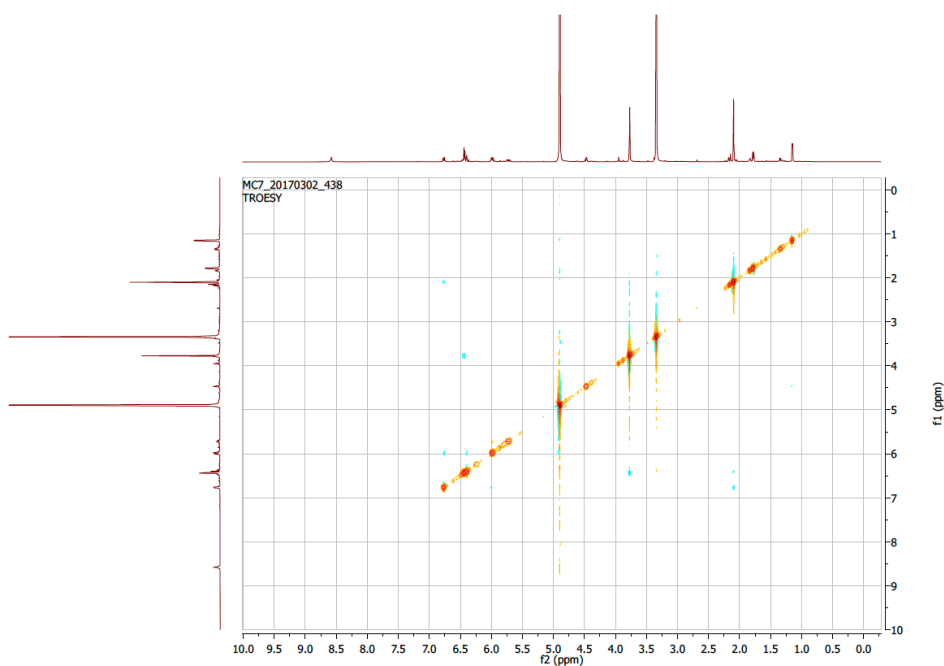
COSY spectrum of **5** in CD₃OD (500 MHz).



HSQC spectrum of **5** in CD₃OD (500 MHz).



HMBC spectrum of **5** in CD₃OD (500 MHz).



TROSY spectrum of **5** in CD₃OD (500 MHz).

Reference:

1. Sato M et al. (2017) Collaborative biosynthesis of maleimide- and succinimide-containing natural products by fungal polyketide megasynthases. *J Am Chem Soc* 139:5317-5320.
2. Ma SM et al. (2009) Complete reconstitution of a highly reducing iterative polyketide synthase. *Science* 326: 589-592.
3. Crawford JM et al. (2008) Acyl-carrier protein-phosphopantetheinyltransferase partnerships in fungal fatty acid synthases. *ChemBiochem* 9: 1559-1563.
4. Britton HTS, Robinson RA (1931) The use of the antimony-antimonous oxide electrode in the determination of the concentration of hydrogen ions and in potentiometric titrations. The Prideaux-Ward universal buffer mixture. *J Chem Soc* 0:458-473
5. Porra RJ, Thompson WA, Kriedemann PE. (1989) Determination of accurate extinction coefficients and simultaneous equations for assaying chlorophylls a and b extracted with four different solvents: verification of the concentration of chlorophyll standards by atomic absorption spectroscopy. *Biochimica et Biophysica Acta* 975:384-394.